

QUBIC IV: Performance of TES Bolometers and Readout Electronics

M. Piat¹ G. Stankowiak¹ E.S. Battistelli^{2,3} P. de Bernardis^{2,3}
G. D'Alessandro^{2,3} M. De Petris^{2,3} L. Grandsire¹ J.-Ch. Hamilton¹
T.D. Hoang⁴ S. Marnieros⁵ S. Masi^{2,3} A. Mennella^{6,7} L. Mousset¹
C. O'Sullivan⁸ D. Prêle¹ A. Tartari⁹ J.-P. Thermeau¹
S.A. Torchinsky^{1,10} F. Voisin¹ M. Zannoni^{11,12} P. Ade¹³
J.G. Alberro¹⁴ A. Almela¹⁵ G. Amico² L.H. Arnaldi¹⁶ D. Auguste⁵
J. Aumont¹⁷ S. Azzoni¹⁸ S. Banfi^{11,12} B. Bélier¹⁹ A. Baù^{11,12}
D. Bennett⁸ L. Bergé⁵ J.-Ph. Bernard¹⁷ M. Bersanelli^{6,7}
M.-A. Bigot-Sazy¹ J. Bonaparte²⁰ J. Bonis⁵ E. Bunn²¹ D. Burke⁸
D. Buzi² F. Cavaliere^{6,7} P. Chanial¹ C. Chapron¹ R. Charlassier¹
A.C. Cobos Cerutti¹⁵ F. Columbro^{2,3} A. Coppolecchia^{2,3}
G. De Gasperis^{22,23} M. De Leo^{2,24} S. Dheilly¹ C. Duca¹⁵
L. Dumoulin⁵ A. Etchegoyen¹⁵ A. Fasciszewski²⁰ L.P. Ferreyro¹⁵
D. Fracchia¹⁵ C. Franceschet^{6,7} M.M. Gamboa Lerena^{25,26}
K.M. Ganga¹ B. García¹⁵ M.E. García Redondo¹⁵ M. Gaspard⁵
D. Gayer⁸ M. Gervasi^{11,12} M. Giard¹⁷ V. Gilles^{2,27}
Y. Giraud-Heraud¹ M. Gómez Berisso¹⁶ M. González¹⁶
M. Gradziel⁸ M.R. Hampel¹⁵ D. Harari¹⁶ S. Henrot-Versillé⁵
F. Incardona^{6,7} E. Jules⁵ J. Kaplan¹ C. Kristukat²⁸ L. Lamagna^{2,3}
S. Loucatos^{1,29} T. Louis⁵ B. Maffei³⁰ W. Marty¹⁷ A. Mattei³
A. May²⁷ M. McCulloch²⁷ L. Mele^{2,3} D. Melo¹⁵ L. Montier¹⁷
L.M. Mundo¹⁴ J.A. Murphy⁸ J.D. Murphy⁸ F. Nati^{11,12} E. Olivieri⁵
C. Oriol⁵ A. Paiella^{2,3} F. Pajot¹⁷ A. Passerini^{11,12} H. Pastoriza¹⁶
A. Pelosi³ C. Perbost¹ M. Perciballi³ F. Pezzotta^{6,7} F. Piacentini^{2,3}
L. Piccirillo²⁷ G. Pisano¹³ M. Platino¹⁵ G. Polenta^{2,31} R. Puddu³²
D. Rambaud¹⁷ E. Rasztocky³³ P. Ringegni¹⁴ G.E. Romero³³
J.M. Salum¹⁵ A. Schillaci^{2,34} C.G. Scóccola^{25,26} S. Scully^{8,35}
S. Spinelli¹¹ M. Stolpovskiy¹ A.D. Supanitsky¹⁵ P. Timbie³⁶
M. Tomasi^{6,7} C. Tucker¹³ G. Tucker³⁷ D. Viganò^{6,7} N. Vittorio²²
F. Wicek⁵ M. Wright²⁷ and A. Zullo³

¹Université de Paris, CNRS, Astroparticule et Cosmologie, F-75006 Paris, France

- ²Università di Roma - La Sapienza, Roma, Italy
- ³INFN sezione di Roma, 00185 Roma, Italy
- ⁴University of Science and Technology of Hanoi, Vietnam Academy of Science and Technology
- ⁵Laboratoire de Physique des 2 Infinis Irène Joliot-Curie (CNRS-IN2P3, Université Paris-Saclay), France
- ⁶Università degli studi di Milano, Milano, Italy
- ⁷INFN sezione di Milano, 20133 Milano, Italy
- ⁸National University of Ireland, Maynooth, Ireland
- ⁹INFN sezione di Pisa, 56127 Pisa, Italy
- ¹⁰Observatoire de Paris, Université Paris Science et Lettres, F-75014 Paris, France
- ¹¹Università di Milano - Bicocca, Milano, Italy
- ¹²INFN sezione di Milano - Bicocca, 20216 Milano, Italy
- ¹³Cardiff University, UK
- ¹⁴GEMA (Universidad Nacional de La Plata), Argentina
- ¹⁵Instituto de Tecnologías en Detección y Astropartículas (CNEA, CONICET, UNSAM), Argentina
- ¹⁶Centro Atómico Bariloche and Instituto Balseiro (CNEA), Argentina
- ¹⁷Institut de Recherche en Astrophysique et Planétologie, Toulouse (CNRS-INSU), France
- ¹⁸Department of Physics, University of Oxford, UK
- ¹⁹Centre de Nanosciences et de Nanotechnologies, Orsay, France
- ²⁰Centro Atómico Constituyentes (CNEA), Argentina
- ²¹University of Richmond, Richmond, USA
- ²²Università di Roma “Tor Vergata”, Roma, Italy
- ²³INFN sezione di Roma2, 00133 Roma, Italy
- ²⁴University of Surrey, UK
- ²⁵Facultad de Ciencias Astronómicas y Geofísicas (Universidad Nacional de La Plata), Argentina
- ²⁶CONICET, Argentina
- ²⁷University of Manchester, UK
- ²⁸Escuela de Ciencia y Tecnología (UNSAM) and Centro Atómico Constituyentes (CNEA), Argentina
- ²⁹IRFU, CEA, Université Paris-Saclay, F-91191 Gif-sur-Yvette, France
- ³⁰Institut d’Astrophysique Spatiale, Orsay (CNRS-INSU), France
- ³¹Italian Space Agency, Roma, Italy
- ³²Pontificia Universidad Católica de Chile, Chile
- ³³Instituto Argentino de Radioastronomía (CONICET, CIC, UNLP), Argentina
- ³⁴California Institute of Technology, USA
- ³⁵Institute of Technology, Carlow, Ireland
- ³⁶University of Wisconsin, Madison, USA
- ³⁷Brown University, Providence, USA

E-mail: piat@apc.univ-paris7.fr, stankowi@apc.in2p3.fr

Abstract. A prototype version of the Q & U Bolometric Interferometer for Cosmology (QUBIC) underwent a campaign of testing in the laboratory at Astroparticle Physics and Cosmology in Paris. The detection chain is currently made of 256 NbSi Transition Edge Sensors cooled to 320 mK. The readout system is a 128:1 Time Domain Multiplexing scheme based on 128 SQUIDs cooled at 1K that are controlled and amplified by an SiGe Application Specific Integrated Circuit at 40 K. We report the performance of this readout chain and the characterization of the TESs. The readout system has been functionally tested and characterized in the lab and in QUBIC. The Low Noise Amplifier demonstrated a white noise level of 0.3 nV/sqrt(Hz). Characterizations of the QUBIC detectors and readout electronics includes the measurement of I-V curves, time constant and the Noise Equivalent Power. The QUBIC TES bolometer array has approximately 80% detectors within operational parameters. While still limited by micro-physics from the pulse tubes and noise aliasing from readout system, the Noise Equivalent Power is about 2×10^{-16} W/ $\sqrt{\text{Hz}}$, enough for the demonstration of bolometric interferometry.

Contents

1	Introduction	1
2	QUBIC Detection chain	2
2.1	TES	2
2.2	SQUIDs	3
2.3	ASIC	4
2.4	Warm electronics and acquisition software	6
3	Readout tests and characterization	6
3.1	ASIC tests and characterizations	6
3.1.1	Implemented functions	6
3.1.2	Current sources and voltage references	7
3.1.3	Amplifier with 4 multiplexed inputs	8
3.1.4	AC bias current source	9
3.1.5	Multiplexer addressing circuit	10
3.2	SQUIDs tests and characterizations	10
3.2.1	Selection and sorting of SQUIDs at 300 K	10
3.2.2	Tests at Cryogenic Temperature	11
4	TES characterization	12
4.1	Selection process and integration	12
4.2	Critical Temperature	12
4.3	TES normal and parasitic resistances	13
4.4	TES parameters	14
4.5	Power background	16
4.6	Phonon Noise Equivalent Power	17
4.7	Time constants	18
4.8	Noise characterizations	21
4.8.1	Noise in normal and superconducting states	23
4.8.2	Noise in the transition	23
5	Conclusion	29

1 Introduction

QUBIC is an international ground based experiment dedicated to the observation of CMB polarisation. It will be deployed in Argentina, at the Alto Chorrillos mountain site (altitude of 4869 m a.s.l.) near San Antonio de los Cobres, in the Salta province. QUBIC has two configurations: the “Technological Demonstrator” (TD) and the “Full Instrument” (FI). The TD and FI share the same cryostat and cryogenics but the TD has only one-quarter of the 150 GHz TES focal plane (256 TESs), an array of 64 horns and switches and a smaller optical combiner. The QUBIC TD has demonstrated the feasibility of the bolometric interferometry after extensive tests at APC laboratory since 2018. In this paper, we present the main results of this characterization phase on the detection chain.

This paper is organized as follows. An overview of the QUBIC detection chain is given in Section 2. The tests of the readout system is described in Section 3. Section 4 describes the TES characterizations in terms of critical temperature, TES parameters, power background, time constants and Noise performances. Finally, some concluding remarks are given in Section 5.

2 QUBIC Detection chain

The QUBIC detection chain architecture is shown on Fig. 1. Each focal plane is composed of four 256-pixel Transition Edge Sensor (TES) arrays assembled together to obtain 1024-pixel detector cooled at about 320 mK by a ^3He fridge. For each quarter focal plane, two blocks of 128 SQUIDs (Superconducting Quantum Interference Devices) are used at 1 K in a 128:1 Time Domain Multiplexing (TDM) scheme [1]. Each block is controlled and amplified by an ASIC (Application Specific Integrated Circuit) cooled to 40 K while a warm FPGA (Field Programmable Gate Array) board ensure the control and acquisition of the signal to the acquisition computer.

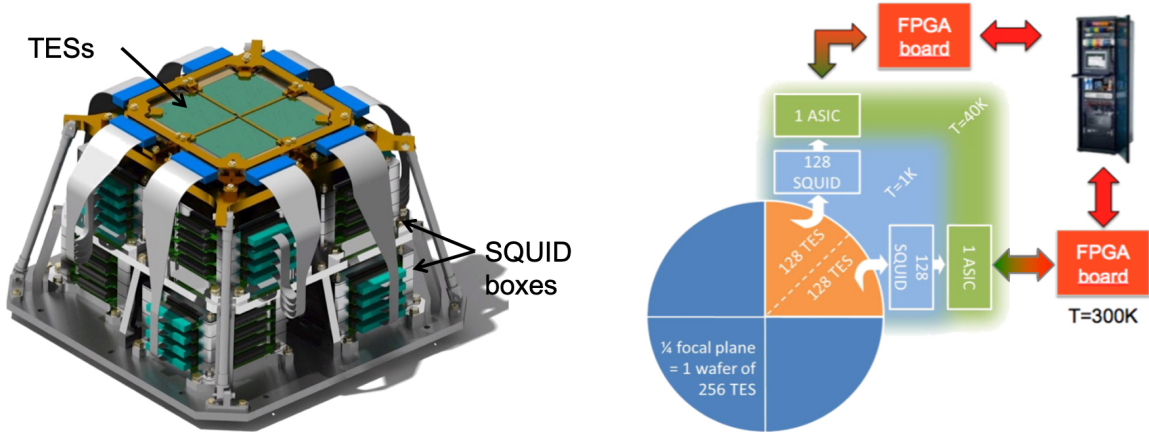


Figure 1. *Left:* QUBIC cryo-mechanical structure which supports one TES focal plane at 350 mK on top and the SQUID boxes at 1 K below. *Right:* Architecture of the QUBIC detection chain for one focal plane of 1024 channels, highlighted on one quarter of it. (Color figure online.)

2.1 TES

The detectors are Transition Edge Sensors made with a $\text{Nb}_x\text{Si}_{1-x}$ amorphous thin film ($x \approx 0.15$ in our case). Their transition temperature T_c (Fig. 2) can be adapted by changing the composition x of the compound. The array currently used (reference P87) has a critical temperature of about 410 mK. The normal state resistance R_n is adjusted to about 1Ω with interleaved electrodes for optimum performances. To adapt to the optics, the pixels have 3 mm spacing while the grid absorber structure is 2.7 mm wide without sensitivity to polarization. The low thermal coupling between the TES and the thermal bath is obtained using 500 nm thin SiN suspended and patterned membranes, which exhibit thermal conductivity in the range 50-500 pW/K depending on the precise pixel geometry and temperature. The Noise Equivalent Power (NEP) is expected to be of the order of $5 \cdot 10^{-17} \text{ W}/\sqrt{\text{Hz}}$ at 150 GHz with a natural time constant of about 100 ms [2]. Light absorption is achieved using a Palladium metallic

grid placed in a quarter-wave cavity optimizing the absorption efficiency. The back-short distance of $400\ \mu\text{m}$ has been chosen after electromagnetic simulations in order to have absorption higher than 94% at both 150 and 220 GHz. The routing of the signal between the TES and the bonding pads at the edge of the array is realised by superconducting Aluminium lines patterned on the Silicon frame supporting the membranes. The detailed fabrication process of the QUBIC detectors is given in [3]. The latest upgrade of the production process allows excellent fabrication quality with a dead pixels yield as low as 5% at room temperature.

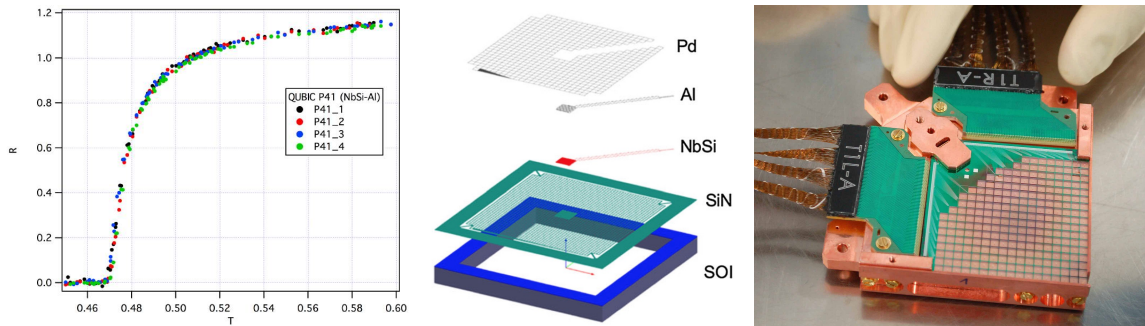


Figure 2. *Left:* Superconducting transition characteristics of four Nb_{0.15}Si_{0.85} TESs distributed far away from each other on the 256 pixel array reference P41. *Middle:* Layout of the 3-mm pitch pixel structure. Pd grid for light absorption, NbSi for temperature sensing, SiN structure for decoupling the sensor from the cold bath and Al for routing the signal to the SQUID amplifiers *Right:* A 256 TES array being integrated.

The 256-pixel array is finally integrated within the focal plane holder and electrically connected to an Aluminium Printed Circuit Board (PCB, provided by Omni Circuit Boards¹) using ultrasonic bonding of Aluminium wires (Fig. 2).

2.2 SQUIDS

The QUBIC detection chain second stage is composed of the Superconducting QUantum Interference Devices (SQUIDS) maintained at a temperature of about 1 K by an ⁴He fridge. Each TES is in series with the input inductance L_{in} of the SQUID and is voltage biased with a $10\ \text{m}\Omega$ resistor in parallel as shown in Figure 3. The input inductance of the SQUID converts the TES current into a magnetic flux Φ_{in} that is converted in an output voltage by the SQUID. The later is therefore a trans-impedance amplifier with a gain of the order of 100 V/A.

To compensate the flux variation, a current from a feedback loop is injected to create a feedback flux Φ_{fb} . The voltage sent by the DAC to create this feedback current is *in fine* the QUBIC signal (Fig. 3). This process, allowing to lock the flux operating point in the SQUID is known as a Flux Locked Loop [4].

In addition of being a cryogenic amplifier, SQUIDS also enable the multiplexing because of their large bandwidth. As shown in Figure 4, the SQUID multiplexer is composed of 4 columns of 32 SQUIDS AC-biased with capacitors in order to reduce power dissipation and noise.

¹www.omnicircuitboards.com

The SQUIDs used in QUBIC shown in Figure 5 have a dual-washer gradiometric layouts. They are based on a SQ600S commercial design provided by StarCryoelectronics², slightly modified in order to reduce the area of each dies.

Visual inspections and room temperature tests with a probe-station are used to select the SQUIDs before integration on a specific PCB. One SQUID PCB is composed of 32 SQUIDs and is integrated in an aluminium box. The architecture therefore uses 4 of these PCB boxes to read out 128 pixels. As shown in Fig. 1, a stack of 8 SQUID boxes is installed at 1 K below the TESs in the cryo-mechanical structure, surrounded with a Cryophy³ magnetic shield.

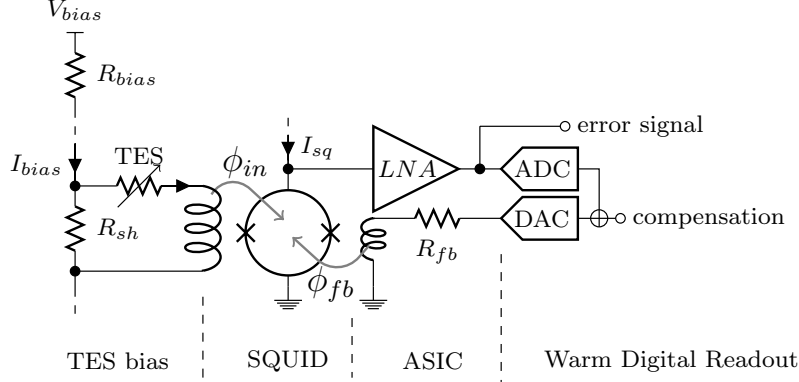


Figure 3. Layout of the TES, SQUID and ASIC operating in flux-locked loop

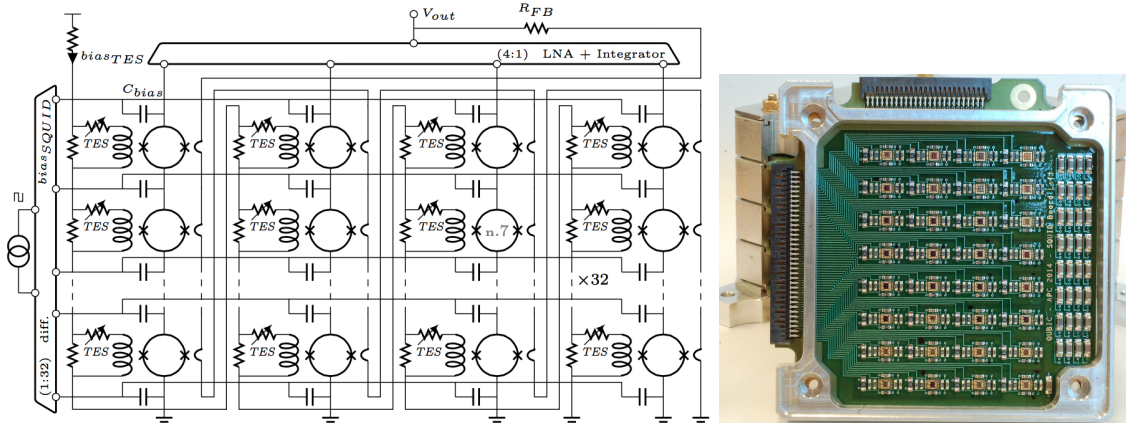


Figure 4. *Left:* Topology of the 128 to 1 multiplexer sub-system (4×32 SQUIDs + 1 ASIC). *Right:* Integration of 32 SQUIDs (1 column) with bias capacitors and filter devices.

2.3 ASIC

In addition to the SQUIDs, a 4 to 1 multiplexed low noise amplifier (LNA) reads out sequentially 4 columns of 32 SQUID each. The resulting multiplexing factor is 128. The LNA, together with sequential biasing of the SQUID and the overall clocking of this 128:1 multiplexer, is all done in a cryogenic ASIC operating at about 40 K [5]. The TDM readout is

²starcryo.com

³www.aperam.com

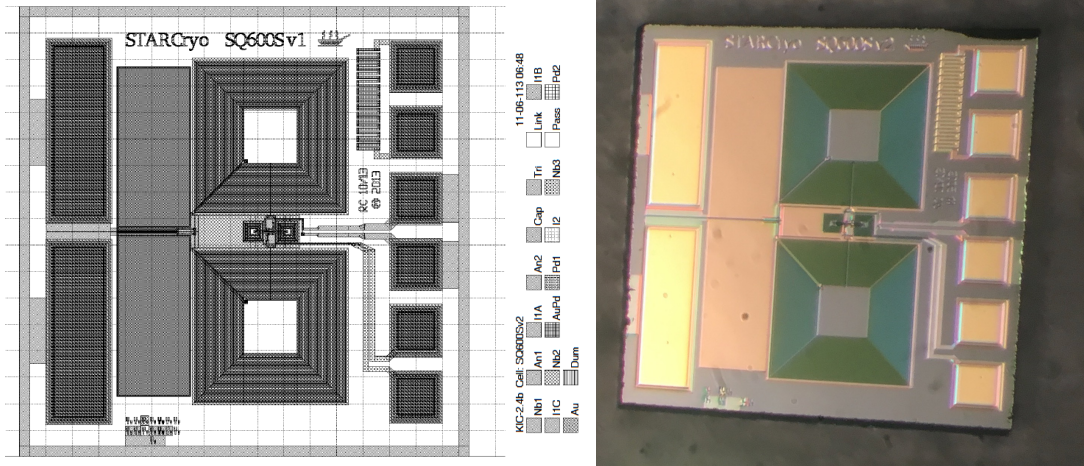


Figure 5. On the left, layout of a gradiometric SQUID (100 μm grid), on the right, picture of one SQUID bare die (about 1.7 mm side).

based on the association of 4 columns of 32 SQUIDs in series with the dedicated cryogenic ASIC.

The ASIC is designed in full-custom using CADENCE CAD tools. The used technology is a standard $0.35\mu\text{m}$ BiCMOS SiGe from Austria MicroSystem (AMS). This technology consists of p-substrate, 4-metal and 3.3 V process. It includes standard complementary MOS transistors and high speed vertical SiGe NPN Hetero-junction Bipolar Transistors (HBT). Bipolar transistors are preferentially used for the design of analog parts because of their good performances at cryogenic temperature [1]. The design of the ASIC is based on pre-experimental characterizations results, and its performance at cryogenic temperature is extrapolated from simulation results obtained at room temperature, using CAD tools.

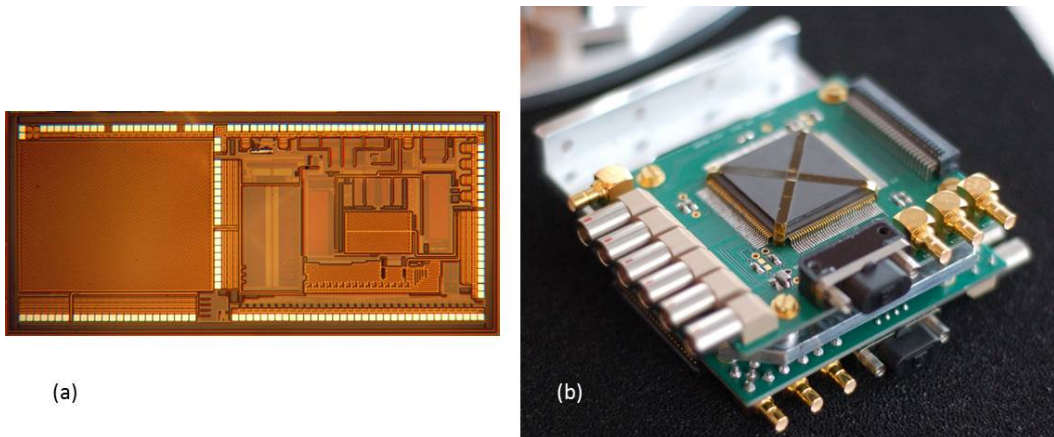


Figure 6. *Left:* Microphotography of the cryogenic ASIC designed to readout 4×32 TES/SQUID pixels. *Right:* ASIC module assembly used for QUBIC experiment.

Each ASIC board for QUBIC (shown in Fig. 6) has a power dissipation of typically 16 mW and is placed on the 40 K stage. The ASIC integrates all parts needed to achieve the readout, the multiplexing and the control of an array of up to 128 TESs/SQUIDs. It includes

a differential switching current source to address sequentially 32 lines of SQUIDs, achieving a first level of multiplexing of 32:1. In this configuration, the SQUIDs are AC biased through capacitors which allows a good isolation (low cross-talk between SQUID columns) and no power dissipation. A cryogenic SiGe low-noise amplifier ($e_n = 0.3 \text{ nV}/\sqrt{\text{Hz}}$, gain = 70, bandwidth of about 6 MHz in simulations) with 4 multiplexed inputs, performs a second multiplexing stage between each column. The 1/f corner frequency of the LNA increases with decreasing temperature. An operation at about 40 K appears to be a good trade-off between this corner frequency and the white noise level.

This cryogenic ASIC includes also the digital synchronization circuit of the overall multiplexing switching (AC current sources and multiplexed low-noise amplifier). A serial protocol allows to focus on sub-array as well as to adjust the amplifiers and current sources with a reduced number of control wires. As the digital side takes a large part, we have developed a full-custom CMOS digital library dedicated to cryogenic applications and ionizing environments (rad-hard full custom digital library) [1].

2.4 Warm electronics and acquisition software

The final stage of the readout electronics operates at room temperature on a board called NetQuiC. It is connected to the acquisition computer via a network switch. Each NetQuiC board is based on a differential amplifier (gain = 100, bandwidth limited to 1 MHz with a second-order anti aliasing low-pass filter), a 2 MHz 16 bits ADC, seven 16 bits DACs and a Xilinx Spartan 6 FPGA (XEM6010 board from Opal Kelly). This system is designed to adjust the operating biasing of the TESs and to control the feedback of the SQUIDs. Moreover, it takes the signal from the cryogenic multiplexing ASIC, computes the scientific signal and sends it to the data acquisition system. For this detection chain each FPGA manages 128 detectors, with a total of 16 FPGAs for the full 2048 pixel focal planes. A dedicated software named QUBIC Studio was developed at the Institute for Research in Astrophysics and Planetology (IRAP) for the data acquisition [6]. QUBIC Studio interfaces with the generic Electrical Ground Support Equipment (EGSE) tool, called “Dispatcher”, which was also developed at IRAP. QUBIC Studio has a user-friendly interface to manage the connection with the readout electronics. This tool gives a global visualization of the complete detection chain.

3 Readout tests and characterization

The core of the readout is made of an ASIC cooled to 40 K that controls the multiplexing and amplifies the voltage from the SQUIDs. This device has been first tested and validated since it has been used to further characterize the SQUIDs.

3.1 ASIC tests and characterizations

3.1.1 Implemented functions

The ASIC *SQMUX128evo* has been designed to control the time-domain multiplexing and to amplify the signals from 4 columns of 32 SQUIDs in series (see Fig. 4) i.e. 128 channels. Its block diagram is outlined on Figure 7. The following functions have been integrated:

- An ultra low noise voltage amplifier with 4 multiplexed inputs for reading 4 columns of SQUIDs,

- a current source for the polarization of the multiplexed amplifier,
- an AC bias current source associated with a 1:32 multiplexer for addressing the 32 SQUIDs lines through addressing capacitors,
- two voltage references for adjusting the common mode at the input of the multiplexed amplifier and at the output of the AC bias source of the SQUID,
- a digital circuit which controls the row / column addressing of the multiplexer from an external clock signal CK,
- a serial link for addressing configurable blocks such as voltage references, bias current sources or the multiplexer's row/column addressing circuit.

This ASIC has been made in standard BiCMOS SiGe 0.35 μm AMS technology and is powered at 3.3 V. It has been integrated on a specific PCB in order to be fully characterized at room and cryogenic temperatures. The ASIC has been tested and proven functional down to 4.2 K thanks to a low power dissipation of about 16 mW per ASIC whatever the number of columns to read out is. In QUBIC, the ASIC operates at approximately 40 K due to the available cryogenic power.

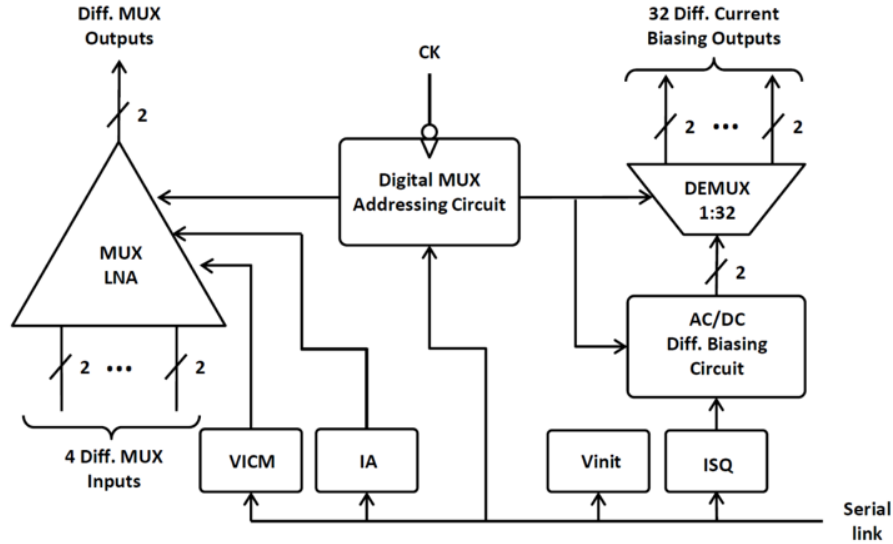


Figure 7. Block diagram of the ASIC *SQMUX128evo* (see text for a detailed description).

3.1.2 Current sources and voltage references

The ASIC called *SQMUX128evo* integrates digitally adjustable current sources and voltage references for the biasing of the multiplexed input amplifier and for the SQUID AC bias circuit. The current sources are based on a fixed current reference ($I_{REF} \simeq 100 \mu\text{A}$ typically) followed by current DACs whose values are encoded on 3 and 4 bits for the amplifier bias and the SQUID AC bias circuit respectively. The reference current I_{REF} is obtained by taking the current flowing through an external resistor R_{REF} under a fixed voltage (forward-biased diode voltage, about 0.7 V at room temperature). This allows to precisely adjust

the reference current value according to the operating temperature. For a nominal current $I_{REF} = 100 \mu\text{A}$:

- The output of the 3-bits current DAC allows to adjust the bias of the amplifier with multiplexed inputs (IA in Fig. 7) from 1.65 mA to 2.85 mA in steps of 200 μA ;
- The output of the 4-bits DAC in current adjusts the AC bias of the SQUIDs (ISQ in Fig. 7) from 5 μA to 40 μA in steps of 2.5 μA (referred to as indexes from 0 to 15 in the following).

The ASIC *SQMUX128evo* also incorporates two 3-bits voltage references for common mode adjustment at the input of the multiplexed amplifier (VICM) and at the output of the SQUID AC bias source (Vinit). This voltage ranges from 1.453 mV to 1.895 mV.

For the voltage references and current sources, the values measured at room temperature are fully compliant to those simulated. At low temperatures, an adjustment of the reference resistance and of the threshold voltage of a forward-biased diode from 0.7 V to about 1 V needs to be done to reproduce the results in simulation for the current sources. The agreement between measurement and simulation can be explained by the fact that the technology used is a proven standard technology with a reliable design kit.

3.1.3 Amplifier with 4 multiplexed inputs

The amplifier is made of 4 differential pairs of SiGe bipolar transistors (each with a transconductance g_m) whose collectors are connected to a common resistor ($R_L = 560 \Omega$ at room temperature and 500Ω at 40 K). The multiplexing is achieved by means of a set of CMOS switches that sequentially bias each differential pair that has to be activated ($I_{BIAS} = 2 \text{ mA}$ typically). A common mode (VICM) is applied at the input of each differential pair through 2 series resistors of 50Ω each (differential input impedance of 100Ω) connected to a 3-bit voltage reference. Each output of the differential stage is followed by a common collector amplifier in order to reduce the output impedance to about 50Ω at low temperature. The expected maximum gain is about 20 and 70 at room and cryogenic temperature respectively.

Gain and noise measurements were performed using an Agilent⁴ HP89410 vector analyser. For the gain measurement, as the vector analyser does not have differential sources and inputs, the setup uses a "single to differential" circuit, made from an AD8132, to differentiate the signal coming from the analyser source and drive the input of the amplifier under test. The output common mode of the AD8132 is adjusted to match the VICM of the amplifier under test. A Stanford Research SR560 amplifier is used to differentiate between the outputs of the amplifier under test before feedback to the input of the analyser. This external amplifier limits the bandwidth to about 1 MHz. For noise measurement, this amplifier is also used to provide the extra gain needed to overcome the noise floor of the analyser. In addition, the noise measurement is performed by shunting the differential inputs of the amplifier under test with a short circuit in the lab or with zero bias of the SQUIDs in QUBIC. The amplifier with multiplexed inputs is biased at maximum current (1.80 mA at 300 K and 2.85 mA at 77 K) so that the voltage gain is as high as possible.

From 300 K to 77 K, the voltage gain increases from 20 to 70 as expected and the white noise level decreases from $0.95 \text{ nV}/\sqrt{\text{Hz}}$ to $0.25 \text{ nV}/\sqrt{\text{Hz}}$ as shown in figure 8. The corner frequency also increases from about 100 Hz at room temperature to about 6 kHz at 77 K. The presence of an excess noise below 10 Hz at low temperature is not understood. The 3 dB

⁴<http://www.agilent.com>

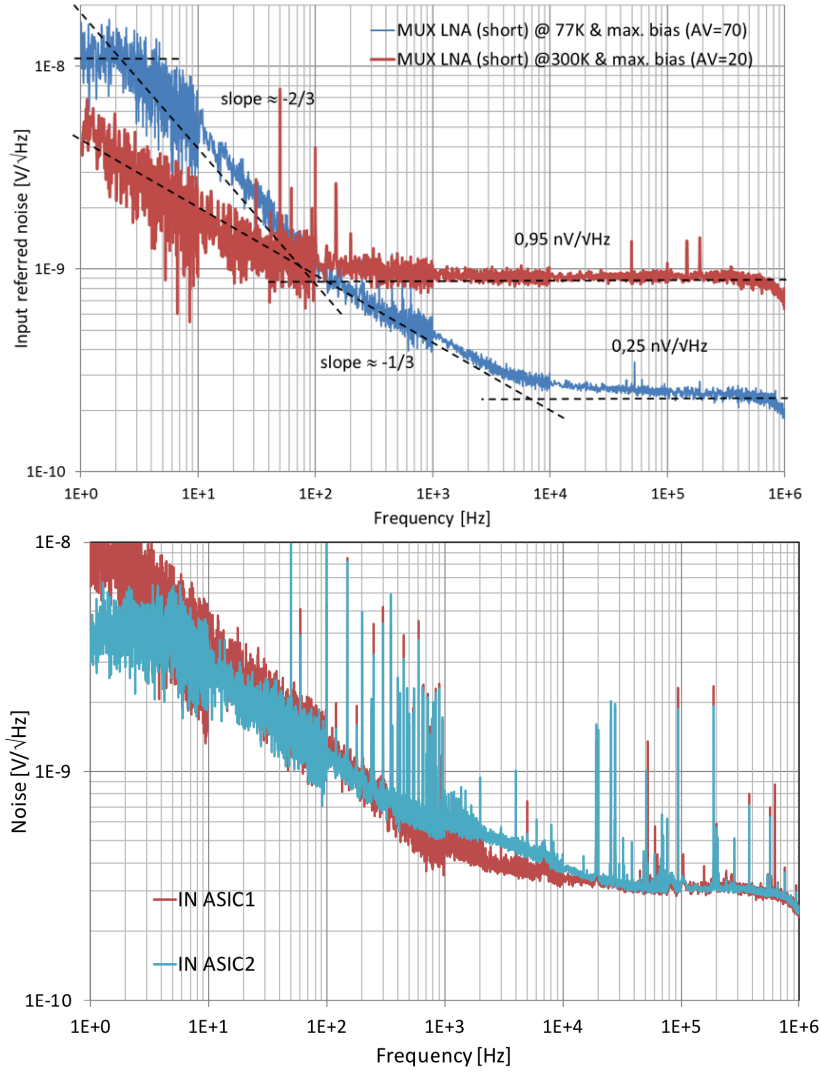


Figure 8. Multiplexed LNA (low noise amplification) equivalent input noise voltage measurement at 300 and 77 K (top) and at 77 K for the two ASICs in QUBIC (bottom).

bandwidth of the LNA is estimated at about 10 MHz by simulation, not measured precisely because of the limitation from the measurement setup.

3.1.4 AC bias current source

The AC bias current source allows to alternately bias two consecutive SQUIDs of the same row at $+I_{sq}$ and $-I_{sq}$ through addressing capacitors (no power dissipation on the cryogenic stages as compared to the addressing with resistors). It consists of two differential branches, each of them having an inverter degenerated by current mirrors referenced to the biasing current source described above. These inverters are controlled in phase opposition to the rate imposed by the column changes. Alternately, the outputs of these inverters simultaneously push and pull the same I_{sq} biasing current through each SQUID of the same row through the addressing capacitors. A 1:32 multiplexer located at the output of the inverters of the AC

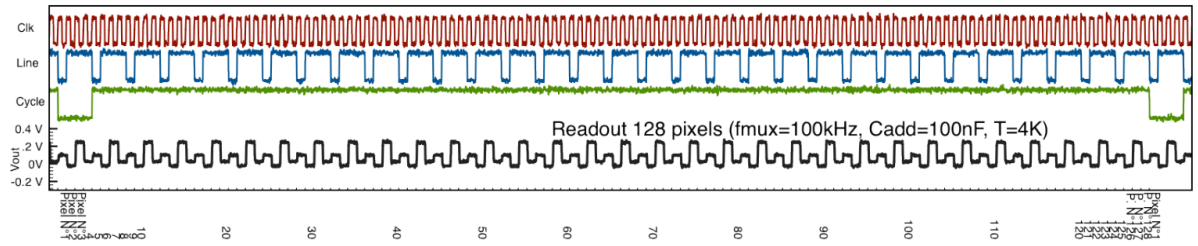


Figure 9. Functional clocking validation at 4.2K of the multiplexer: Clk: clock; Line: synchronize the SQUID switching current source to the multiplexed LNA; Cycle: give the start - pixel 1 - of the full multiplexing cycle; Vout is the multiplexed signal of 128 pixels with the SQUID stage replaced by 128 resistors biased through capacitors. 4 different offsets are noticeable).

source allows the selection of the row to be biased. In order to avoid a drift of the operating point at the output of the inverters of the AC biasing circuit and a risk of saturation of the current sources, these outputs are connected to the voltage reference V_{init} through 2 external resistors of 10k Ω .

3.1.5 Multiplexer addressing circuit

The sequencing of the multiplexing is carried out internally of the ASIC by an integrated digital circuit referenced to an external clock signal CK of 100 kHz maximum frequency. In addition to the control of the LNA and the SQUID biasing circuit, it generates two signals actives on falling edge, SYNCCb and SYNCLb, that indicate the end of row and complete cycle respectively.

Functional tests of the ASIC have been performed down to 4.2K on a small array of 2 columns of 2 SQUIDs in series as shown in figure 9. These tests have validated the AC SQUID biasing operation and the overall multiplexing topology (switching AC current sources, multiplexed LNA and digital clocking).

3.2 SQUIDs tests and characterizations

The SQUIDs are first selected with room temperature measurements and furthermore characterized at two temperature in the QUBIC readout system.

3.2.1 Selection and sorting of SQUIDs at 300 K

Before installation in QUBIC, the manufactured SQUIDs undergo a visual inspection in a clean room in order to detect and remove the ones exhibiting evidence of defects during fabrication or storage. We further proceed in the measurement of 4 resistance values at room temperature: heater, SQUID washer, feedback inductance and input inductance. A histogram of the measured values is plotted in Figure 10. SQUIDs with all parameters within 2σ of the mean values are selected for installation in QUBIC. SQUIDs that are between 2σ and 3σ for one or more measurements are held aside as a possible option in case there are not enough SQUIDs passing the first criteria. All SQUIDs with any parameter larger than 3σ from the mean are rejected. A further selection process is performed based on the leakage resistance between SQUID washer and the input inductance. Leakage measured at cryogenic temperature is typically a few M Ω between a full stack of 32 SQUIDs and the 32 input inductances. This level of leakage does not significantly degrade the operation of the SQUIDs. The pass/fail level for leakage to the input inductance was therefore set at

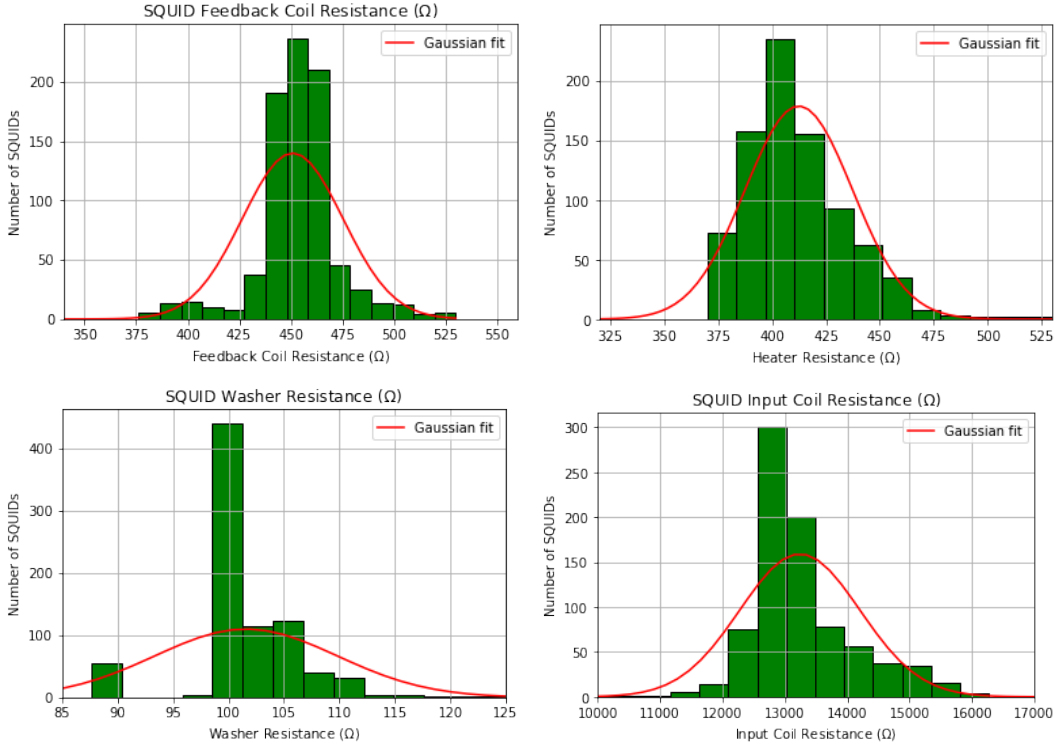


Figure 10. Plot of the measured resistance element values of the SQUIDs at room temperature (Ohms). From left to right : (a) feedback coil, (b) heater, (c) SQUID washer, (d) input coil

2 M Ω , with the majority of leakage values measured closer to 20 M Ω . SQUIDs with leakage to the input inductance less than 2 M Ω were rejected. The leakage between the SQUID washer and the feedback must be that of an open circuit (resistance > 40M Ω), otherwise the SQUID is rejected. We typically obtained a yield of about 82% for tested SQUIDs.

3.2.2 Tests at Cryogenic Temperature

The characterization of the SQUIDs is performed at the beginning of the calibration phase. The main goal is to define the optimal SQUID bias current to be used during observations.

The principle of the procedure is the following: an input sinusoidal signal of 1 V peak-to-peak amplitude is injected into the feedback inductance through the feedback resistor R_{fb} and the bias current of the SQUIDs is increased step by step. For each value of the input current I_{sq} , the response of the SQUID is therefore measured as shown in Figure 11.

As the SQUID current I_{sq} increases, the amplitude of the response of the SQUID also increases until it reach a maximum and then it decreases. The optimum I_{sq} corresponds to the maximum amplitude of the SQUID response. Since the same I_{sq} must be supplied to all SQUID per ASIC, it is necessary to select a single bias index for all the SQUIDs for each ASIC. While it seems natural to choose the SQUID current bias corresponding to the majority of the SQUIDs, in reality it does not maximize the number of operational SQUIDs. A SQUID is considered operational if its response is greater than 10 μ V. The SQUID current is therefore chosen to maximize the number of operational SQUIDs. Figure 12 shows the histograms of the SQUID response for three I_{sq} bias current for the two ASICs.

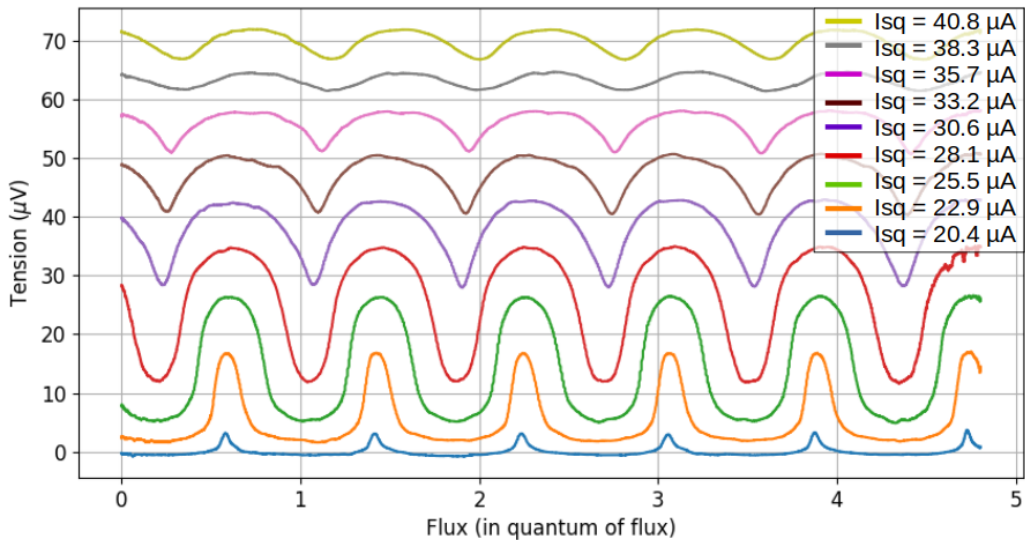


Figure 11. Flux to voltage SQUID transfer function for current biasing on ASIC 1. The plots show the response signal (V_{sq}) as a function of the quantum flux going through the SQUID. There are 9 curves corresponding to increasing bias current (I_{sq}) from bottom to top.

The histograms of Figure 12 show that index 10 ($28 \mu\text{A}$) is the best bias index for ASIC 1 for which 93% of the SQUIDS are operational. For ASIC 2, the histograms give index 11 ($30.6 \mu\text{A}$) as the best bias index with 91.1% operational SQUIDS.

The yield of SQUIDS for the QUBIC Technological Demonstrator is 93% for the 128 SQUIDS connected to ASIC 1, and 89% for the 128 SQUIDS connected to ASIC 2. This corresponds to 119 operational SQUIDS for ASIC 1 and 114 operational SQUIDS for ASIC 2. The total yield is therefore 91%. The optimum bias current is $28.1 \mu\text{A}$ for ASIC 1 (bias index 10) and $30.6 \mu\text{A}$ for ASIC 2 (bias index 11).

4 TES characterization

The TES array currently used in QUBIC has the reference P87 of the production series. It has been selected after characterizations both at room and cryogenic temperatures. This array has been also fully characterized during the QUBIC calibration phase.

4.1 Selection process and integration

The TES arrays that have been successfully produced undergo visual inspections and resistance measurements at room temperature on a probe station. These measurements are done before integration and wire bonding to detect possible defects or issues with the routing. If successful, the array is integrated in the QUBIC holder and Al wire bonded (Fig. 2).

The next steps consist in characterizations at cryogenic temperature. They are done in an Oxford Instrument dilution fridge before integration in the QUBIC cryostat.

4.2 Critical Temperature

The QUBIC detector wafer includes 8 dark pixels, 4 for each ASIC besides the 124 active ones. These channels consist in NbSi thermal sensors of the same geometry as the ones used

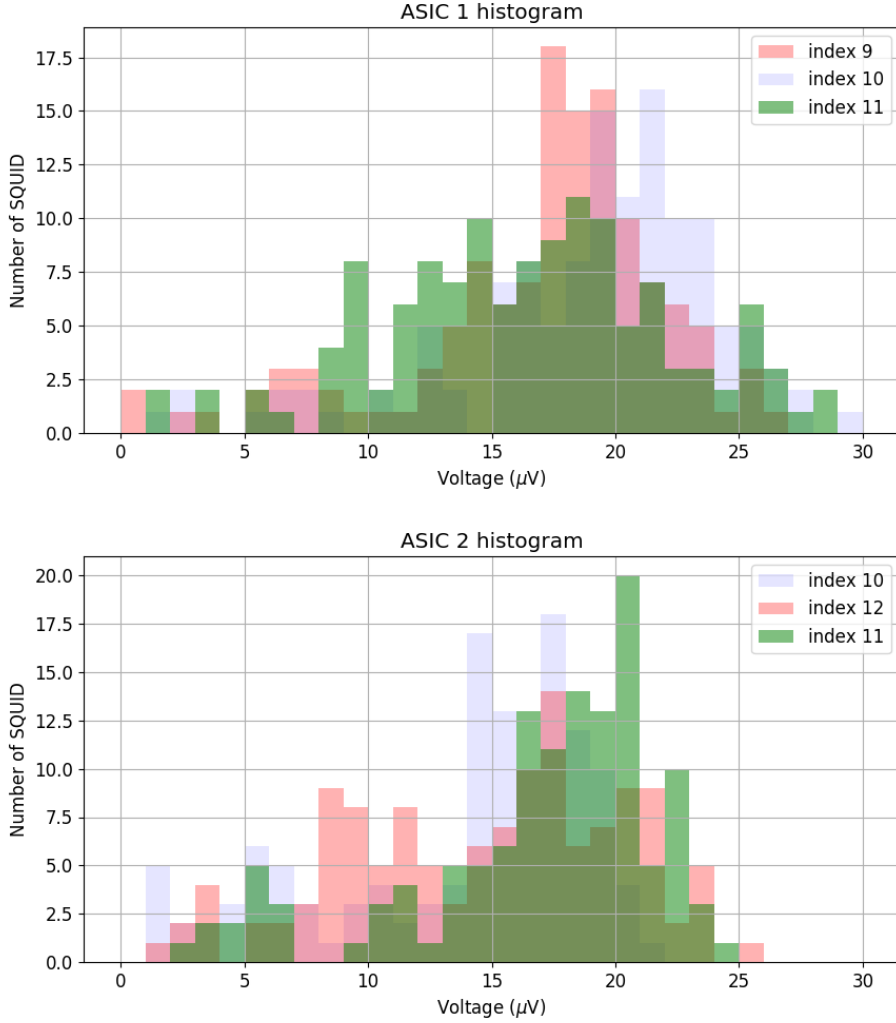


Figure 12. Histogram of voltage swings for SQUIDs on ASIC 1 and 2 for each I_{sq} index corresponding to increasing current.

on TESs, without thermal decoupling from the silicon wafer. They are located outside the focal plane and are therefore shielded from radiation. Figure 13 shows measurements of the transition from normal to superconducting state for 2 of these dark pixels, measured in the dilution fridge by increasing slowly the temperature and with a QUBIC readout chain. The critical temperature is about 412 mK and some temperature dependence is still present above the transition, which allow to still have some sensitivity in case of saturation. The unit-less parameter $\alpha = \frac{T}{R} \times \frac{\partial R}{\partial T}$ has been evaluated from these transition curves and is higher than 100 for the lowest part in the transition.

4.3 TES normal and parasitic resistances

With the bath temperature below the TES critical one, the detectors need to be over-biased (above about $7\mu\text{V}$) in order to be in the normal state. A slow and small sine wave voltage oscillation could be added in order to deduce the resistance value. The same procedure is used to determine the resistance in superconducting state, but without any DC bias on the

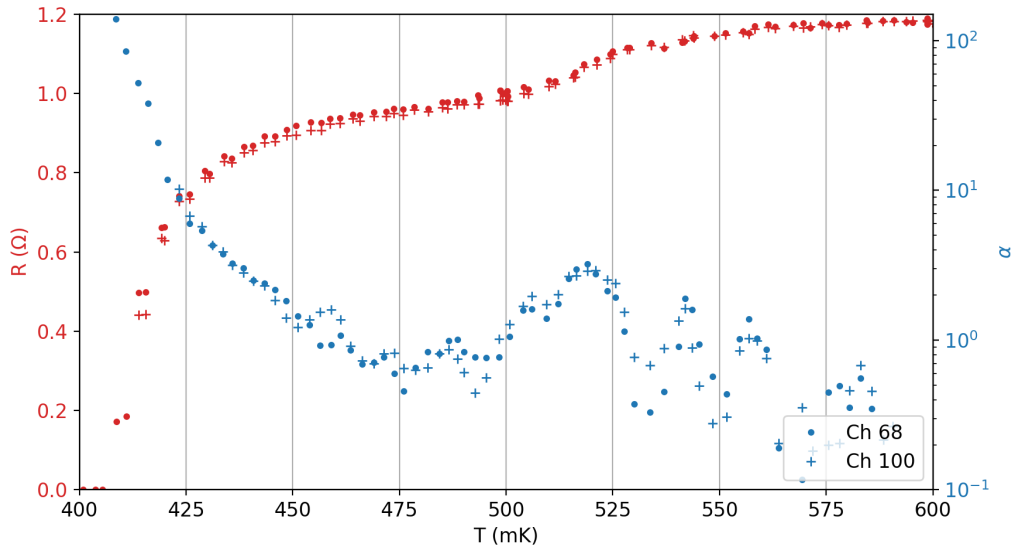


Figure 13. Resistance as a function of temperature for dark pixels on channels 68 and 100 (red) and derived $\alpha = \frac{T}{R} \frac{\partial R}{\partial T}$ parameter (blue).

detectors. The resistance obtained from these measurements, assuming the TES resistance is 0Ω , is given by the sum of the shunt resistance ($10 \text{ m}\Omega$) and the parasitic resistance which is in series with the TES. The parasitic resistance is assumed to come from the connectors used.

Figure 14 shows the distribution of the normal and residual resistance values for the array P87. The normal resistance is highly peaked at about 1.2Ω as expected from the transition measurement. The median residual resistance in superconducting state is about $26 \text{ m}\Omega$. We therefore have a parasitic resistance of about $16 \text{ m}\Omega$ which is compatible with previous measurements on a dedicated test bench.

4.4 TES parameters

The I-V characteristics at different temperatures have been acquired both in the dilution fridge for selection and in the QUBIC cryostat with optical window open and closed. The measurement follows the procedure outlined in [7]. Figure 15 shows the I-V curves for the P87 array measured at 360 mK in blind configuration and Figure 16 is an example of the I-V curves for one TES on ASIC2 at different temperatures. The strong Electro-Thermal Feedback (ETF) regime is clearly seen with the increase of the TES current at low bias voltages. An overall yield of about 84% is furthermore obtained.

The physical parameters of each TES can be deduced from these measurements. Assuming the TES is in the strong ETF regime and that it is blind, the Power-Temperature relation is classically given by:

$$P_{\text{bath}} = \kappa(T_{\text{bath}}^n - T_c^n) \quad (4.1)$$

where P_{bath} is the bias power dissipated in the TES, T_{bath} is the bath temperature, T_c the TES critical temperature, κ and n are constants that depends on the thermal link between the absorber and the bath. In the ETF regime, the bias power is therefore constant for a given bath temperature. The dynamic thermal conductance is further given by the following

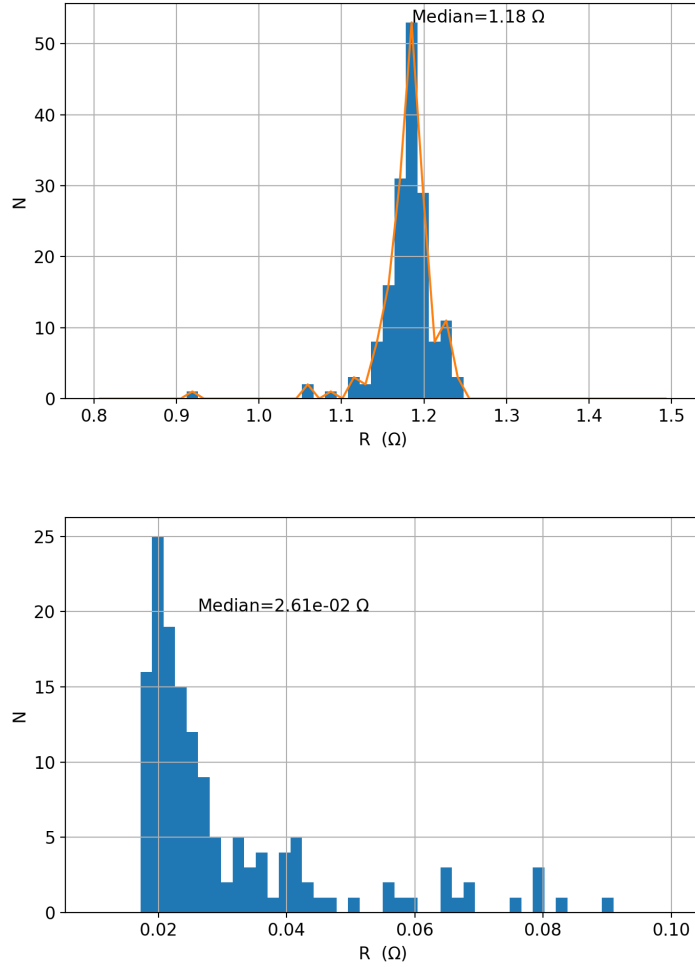


Figure 14. Histogram of normal resistance (top, 168 total number of TES) and of residual resistance in the superconducting state (bottom, 146 total number of TES). This residual resistance is the sum of a parasitic resistance and the bias resistor of 10 mΩ

equation:

$$G(T) = n\kappa T_c^{n-1} \quad (4.2)$$

Figure 17 shows an example of the Power-Temperature relation for the same TES as figure 16. A curve fitting algorithm based on Eq. 4.1 is used to derive the values of κ , n and T_c from measured temperatures and powers.

While degenerate with κ as shown in [2], the index n of the power law is around 4 as expected for a dielectric material. Figure 18 shows the distribution of the critical temperature and dynamic thermal conductance obtained with the fit. The critical temperature is around 410mK as measured on the dark pixels and the median dynamic thermal conductance is about 300pW/K. The spread in these parameters is probably inherent to the previously quoted degeneracy between parameters in the fit.

QUBIC Focal Plane I-V curves: Test cryostat 2018-02-27 and 2018-03-01
 2018-02-27 21:32:35 Array P87 ASIC#1 $T_{\text{bath}}=360.0\text{mK}$
 17 flagged as bad pixels : yield = 86.7%
 2018-03-01 19:20:24 Array P87 ASIC#2 $T_{\text{bath}}=361.9\text{mK}$
 24 flagged as bad pixels : yield = 81.2%
 overall yield 215/256 = 84.0%

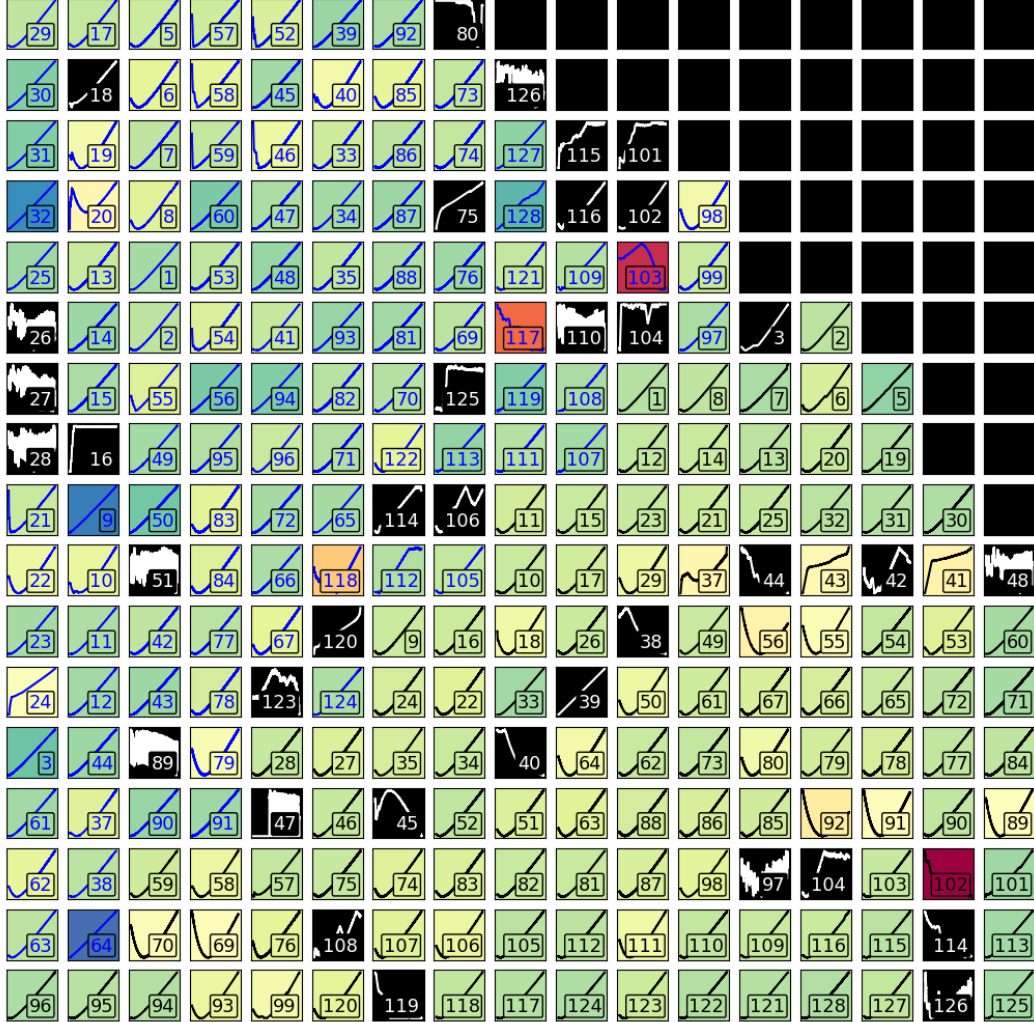


Figure 15. I-V curves of the 244 TES bolometers in the focal plane of the QUBIC Technical Demonstrator. Four TES are outside the focal plane (not shown) and are used as dark detectors for comparison. This is array P87 measured in the APC dilution cryostat at a bath temperature of 360 mK. The background colour indicates the bias voltage turnover point which is the optimal setting. We see homogenous characteristics of the TES array and a yield of 84%.

4.5 Power background

The P-V curves measured during blind characterizations and with the QUBIC optical window open are compared in Figure 19. The comparison leads to an estimate of the power background of the order of 1-2 pW which is in agreement with the photometric model of the instrument since there is a Neutral Density Filter with about 9% transmission at the entrance of the 1K box.

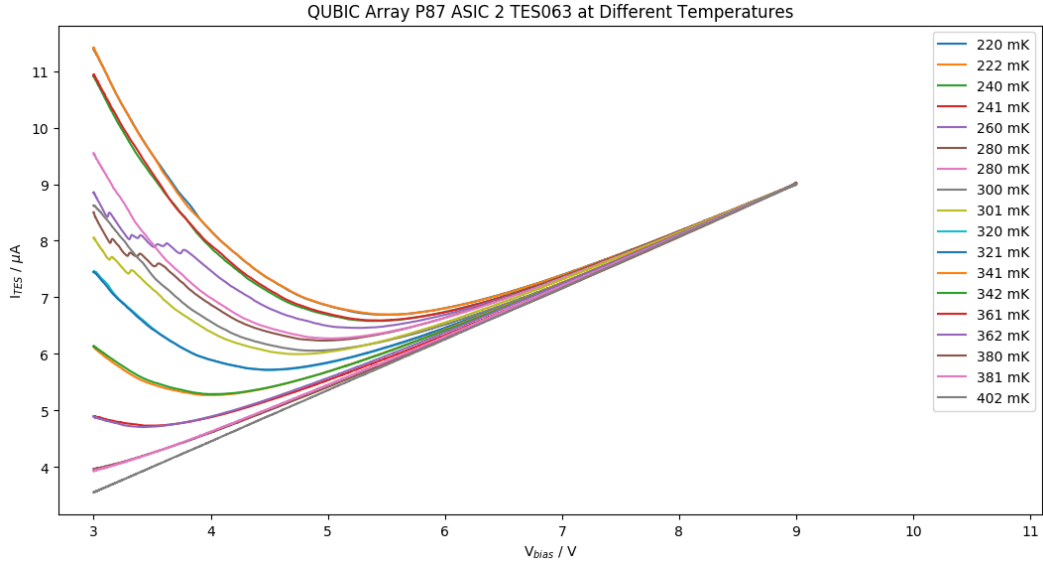


Figure 16. I-V curves of TES#64 on ASIC2 at different temperatures.

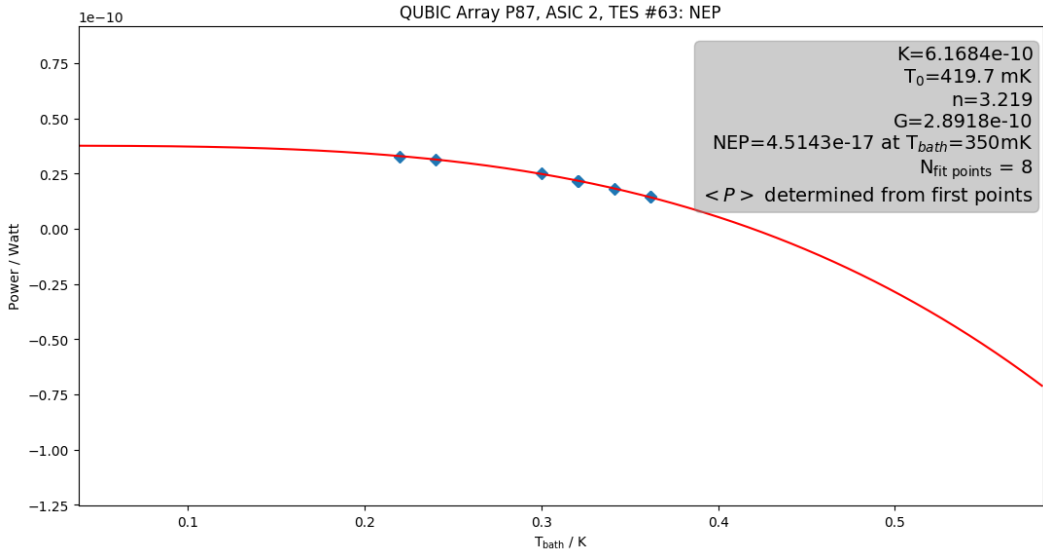


Figure 17. An example of the fit to the Power-Temperature measurements. This is for TES#63 on ASIC2.

4.6 Phonon Noise Equivalent Power

The Phonon Noise Equivalent Power (NEP_{phonon}) was derived from the fitted parameters with the relation [8]:

$$NEP_{\text{phonon}} = \sqrt{\gamma 4k_B T^2 G} \quad (4.3)$$

where k_B is the Boltzmann constant and γ is a correction coefficient given by:

$$\gamma = \frac{n}{2 * n + 1} \frac{1 - \left(\frac{T_{\text{bath}}}{T}\right)^{2*n+1}}{1 - \left(\frac{T_{\text{bath}}}{T}\right)^n}. \quad (4.4)$$

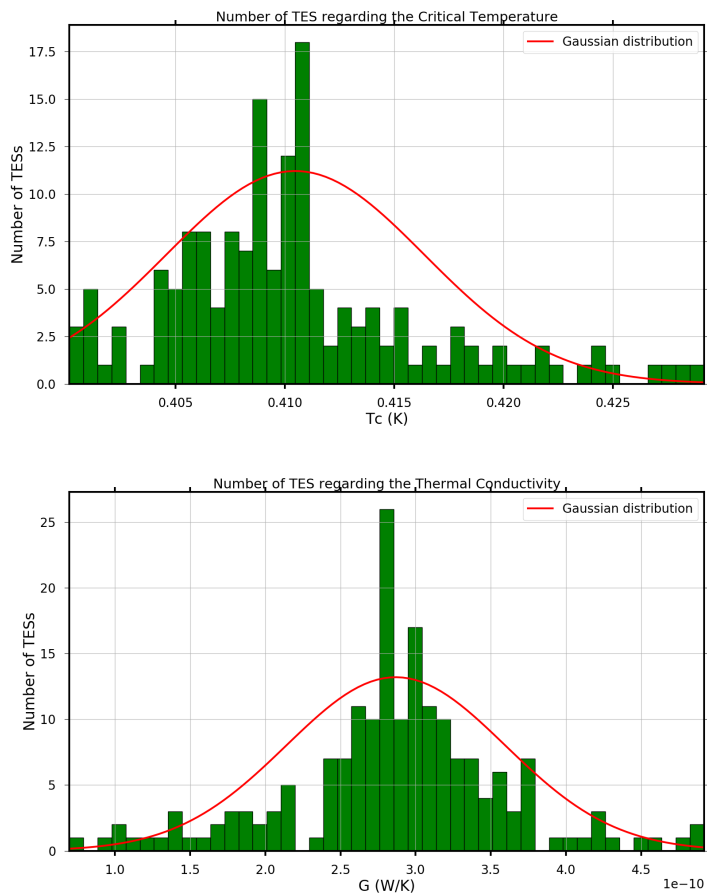


Figure 18. Distribution of critical temperature (top) and dynamic thermal conductance (bottom) of P87 TES array.

Figure 20 shows histograms of the distribution of the phonon NEP values measured for the full array. There is a strong clustering of NEP values around $\sim 4.7 \times 10^{-17} \text{W}/\sqrt{\text{Hz}}$. The dominance of this value in the histogram is an indication of the homogeneity in the fabrication process of the TES array ([9]).

4.7 Time constants

The performances of QUBIC have been tested using a monochromatic calibration source [10]. To estimate the time constants, the calibration source is modulated in power with a square wave signal with a frequency of 0.6Hz and a duty cycle of 33%. The amplitude is adapted to avoid saturation of the detectors while having sufficient signal-to-noise ratio (SNR). The power amplitude on the focal plane is however not constant but corresponds to the synthetic beam. By using a detector located on the calibration source, we checked that the intrinsic rise and fall time is much faster than the expected time constant of the detectors (which is of the order of a few tens of ms).

To process the data, we did a very mild low-pass and high-pass filtering as we do not want the filtering to alter the time constants. We then fold the data for each TES into one

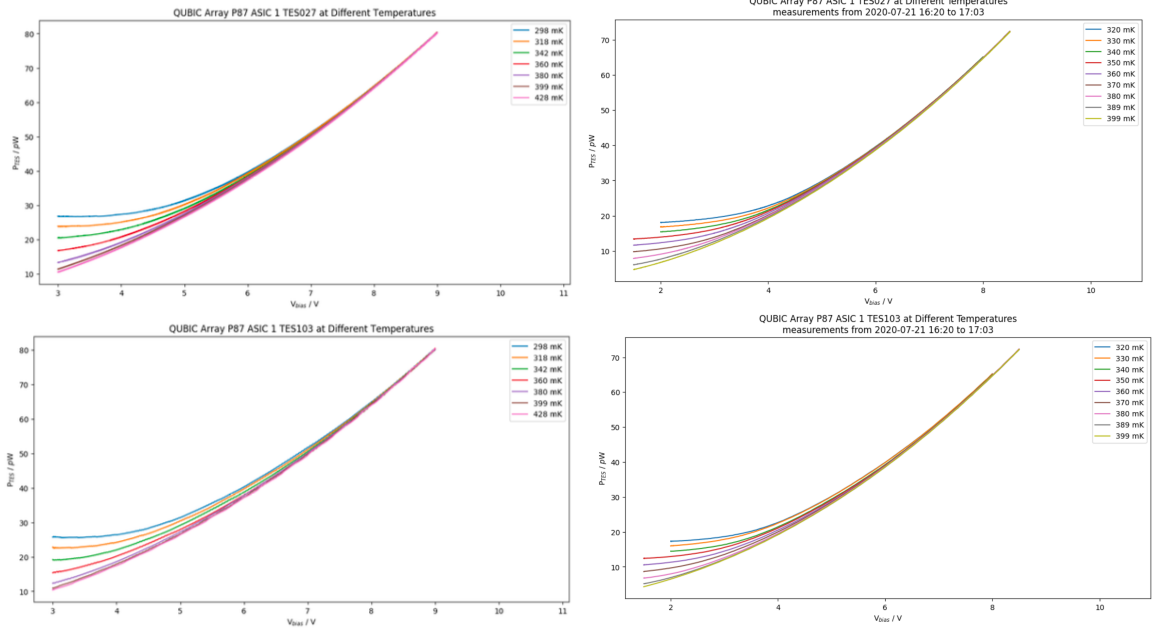


Figure 19. Examples of electrical power P in pW versus bias voltage in V measured in the dilution (left) and in QUBIC (right). Comparing the electrical power at the same bath temperature in the Electro-Thermal Feedback mode (plateau in electrical power) gives the background power.

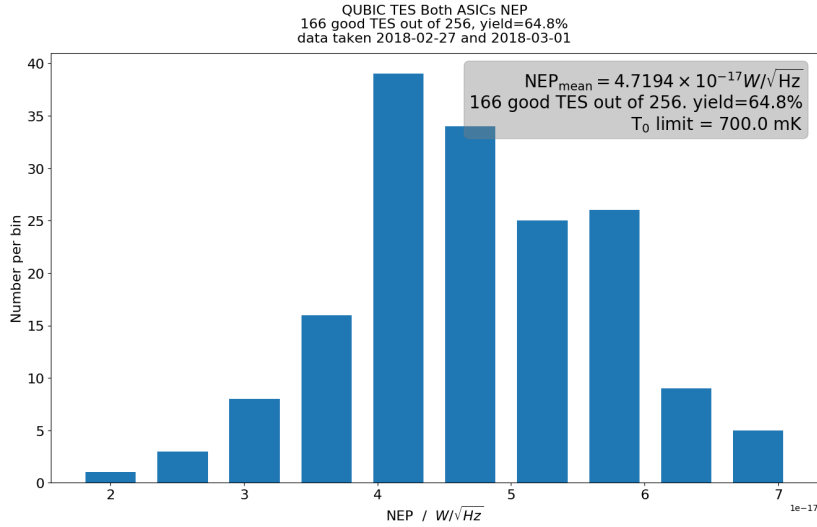


Figure 20. Histogram of the phonon Noise Equivalent Power of the full array. The average phonon NEP is $4.7 \times 10^{-17} \text{W}/\sqrt{\text{Hz}}$.

period of the calibration source. The filtering and the resulting folded signal is shown in Figure 21 for one TES. The signal peaks on the spectrum can be easily seen.

Figure 22 shows the normalized (removed average and divided by RMS) folded data for each TES in black, the median is shown in red. The derivative is shown in blue and helps finding the first guess for the start-time of the calibration source shown as a red dot. Note that no selection has been made at this stage to remove TESs with low SNR.

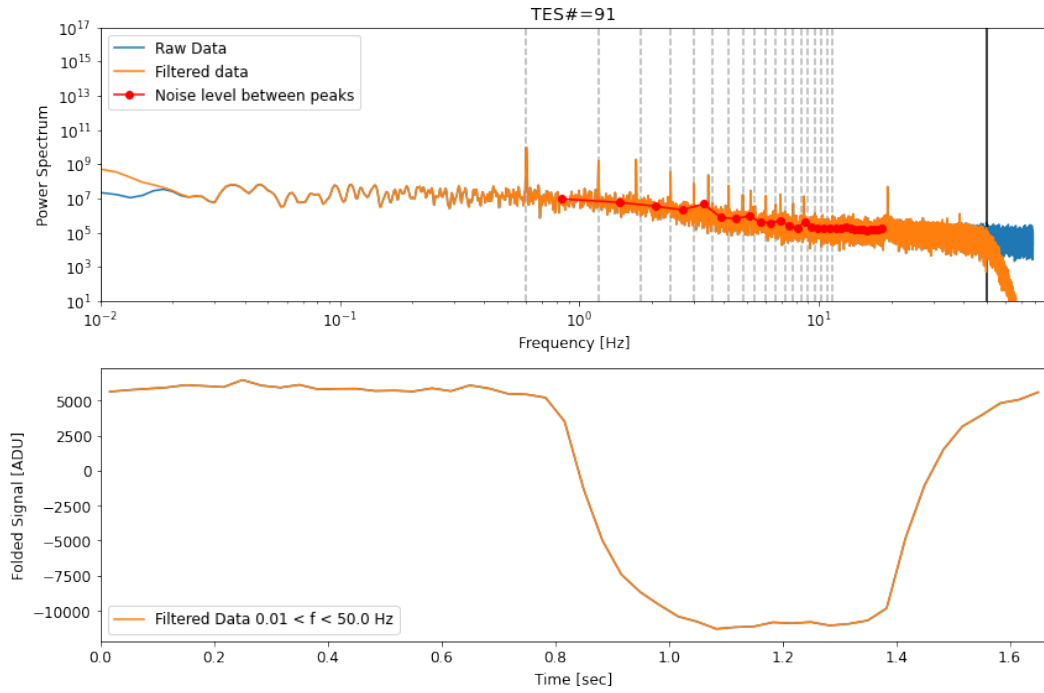


Figure 21. Folded signal for TES#91. upper: The power spectrum in ADU. lower: The folded signal for whole time series.

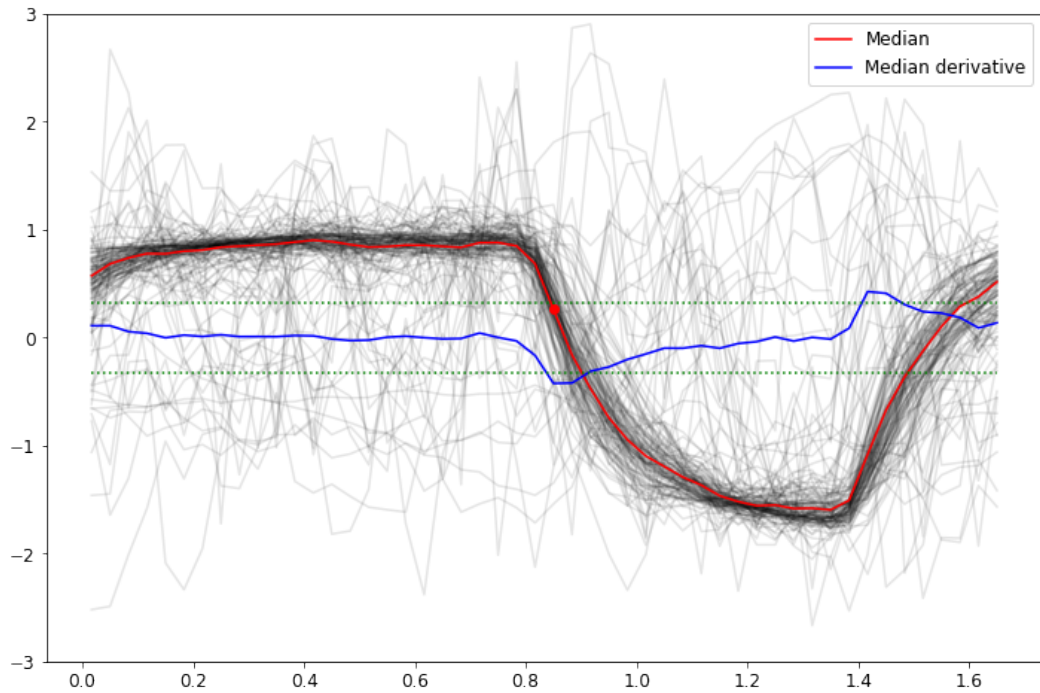


Figure 22. Normalized folded data for each TESs in black, the median is shown in red and its derivative in blue. No selection was done to remove low SNR detectors.

We then fit each TES folded signal (not normalized - meaning with its proper amplitude) with a model for the calibration source signal including a rise time and a fall time.

For each TES, we plot the time constant as a function of the bias voltage V_{TES} (Fig 23).

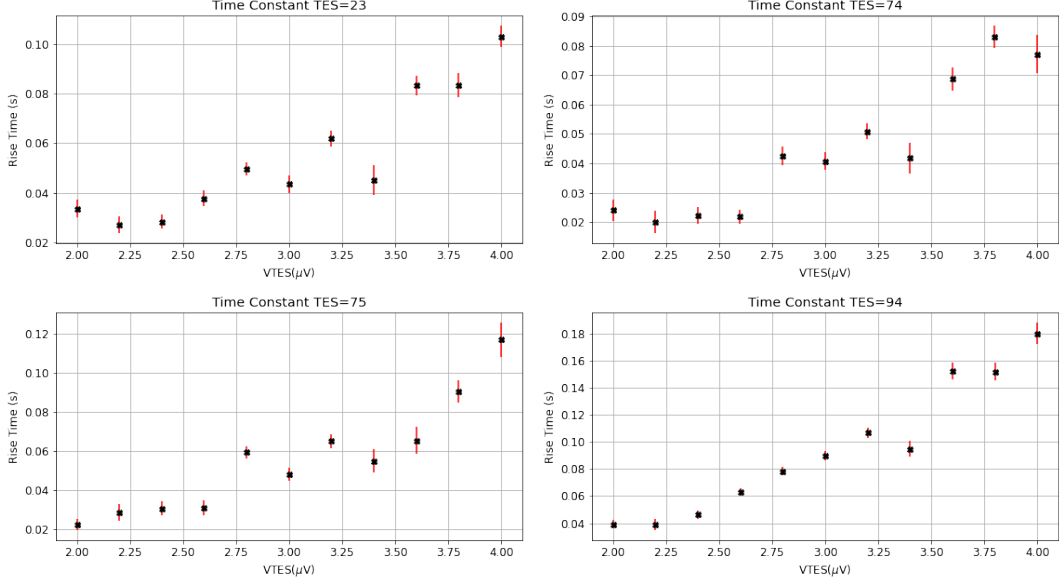


Figure 23. Time constant of four TESs on P87 array in QUBIC.

An important effect, also shown in Figure 24 is the diminution of the time constant at lower bias voltage. As V_{TES} decreases, we have an improvement of the time constant on the detector from about 100ms to 20 ms which is expected from the Electro-Thermal Feedback (ETF) behavior.

Fig. 25 shows the average time constants of all TESs as a function of V_{TES} . The rise time constant appears lower than the fall rime indicating again the effect of ETF, but also the fact that we are probably reaching a non-linear regime for most TESs. For small signals, we expect to have a single time constant reaching at most the value of the rise time measured during this sequence, so about 40 ms. This value is enough for QUBIC since the considered scanning speed is about 1 deg/s which leads to a 30 arcmin beam width duration of 500 ms.

4.8 Noise characterizations

Aliasing of the TES Johnson noise is a limitation to Time Domain Multiplexing performance. Any source of noise before the SQUIDS with a bandwidth higher than the sampling frequency will be aliased. In Time Domain Multiplexing, the signal of each detector is averaged during the duration of measurement T_{meas} which is smaller than the sampling period $T_s = 1/f_s$ by a factor N_{MUX} which is the total number of pixels readout in the multiplexing scheme. The noise bandwidth of this averaging is therefore given by $\Delta f = \frac{1}{2 \times T_{meas}} = \frac{f_s \times N_{MUX}}{2}$. The aliasing leads to an increase of noise given by the square root of the ratio between the noise bandwidth and the Nyquist frequency $f_s/2$ that is $\sqrt{N_{MUX}}$.

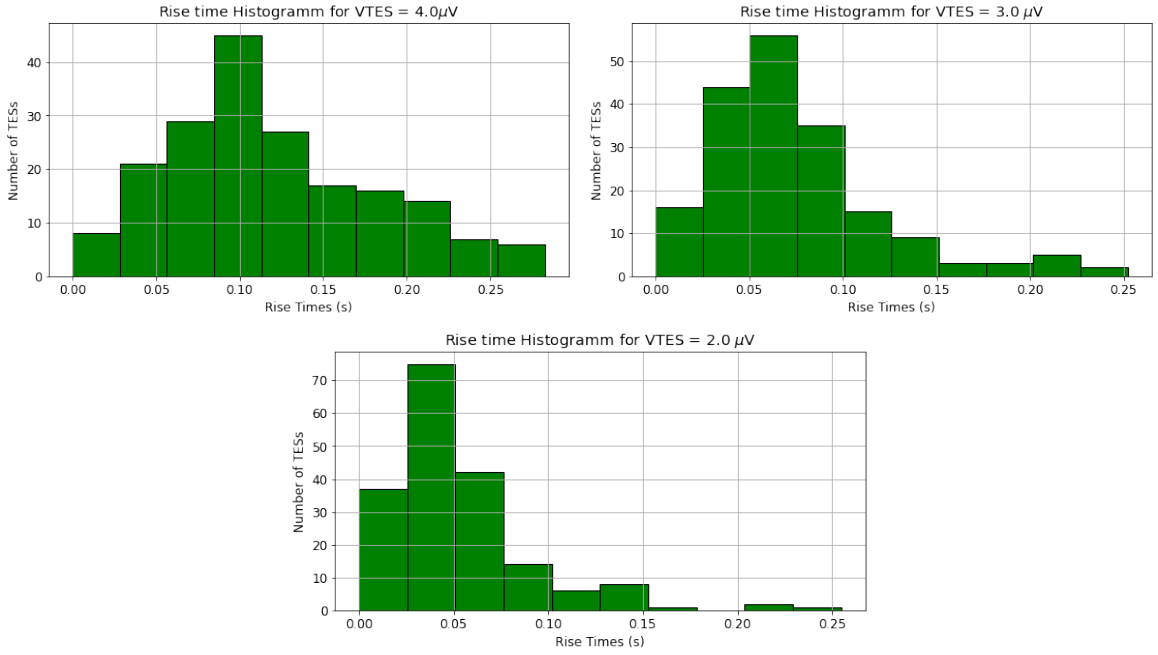


Figure 24. Distribution of the TES time constant for various TES voltage.

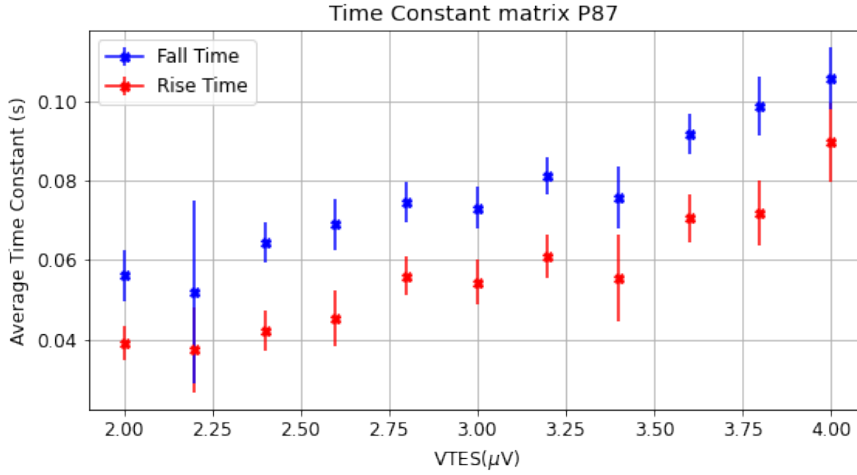


Figure 25. Average value of time constants for rise and fall time as a function of V_{TES} .

In QUBIC, the ADC frequency $f_{ADC} = 2 MHz$ drives the multiplexing. The main parameters are therefore: (i) The number of samples N_s to be read out for each TES, and (ii) the total number of pixels to be read out. The maximum number of pixels is equal to N_{MUX} which is 128. By reducing the number of pixels sampled, the sampling frequency per pixel is increased. The sampling frequency per TES is $f_s = \frac{f_{ADC}}{N_s \times N_{MUX}}$. Typical parameters are $N_s = 100$ and $N_{MUX} = 128$ leading to $f_s = 156.25 Hz$ and $\Delta f = 10 kHz$.

The SQUID input inductance value is $L_{in} = 651 nH$ which leads to a bandwidth higher than 24 kHz for TES resistance above 100 m Ω . For such resistance values, Johnson noise is

increased by a factor $\sqrt{N_{MUX}} = 11.3$. To overcome this limitation, a Nyquist inductor can be added in series with the TES. A value of $L_{Nyq} = 15\mu H$ will reduce the noise bandwidth of Johnson noise to 1 kHz for a 100 m Ω resistance giving an increase of noise of 3.6 for the typical parameters. The number of samples N_s can also be reduced in order to increase the sampling frequency and further reduce the aliasing. This limitation in aliasing was expected for the TD and will be improved for the Full Instrument. The result for the TD is a constraint on NEP of about $10^{-16} W.Hz^{-0.5}$, which is a factor 2 higher than the Full Instrument requirement, but this sensitivity is acceptable for the QUBIC-TD.

4.8.1 Noise in normal and superconducting states

Figure 26 shows the histogram of the measured current noise between 1 Hz and 2 Hz in normal (bias voltage at 8 μV) and superconducting state of the TES. In the normal state, a typical value of 110 $pA.Hz^{-0.5}$ is obtained, compatible with the expectation within a factor of 2 taking into account the aliasing effect. In the superconducting state, the median current noise is 470 $pA.Hz^{-0.5}$, compatible with the expectation taking into account the aliasing effect and the fact that the shunt resistor and probably part of the parasitic resistance are located on the 1 K stage, which was cooled to only about 2.6 K during this measurement.

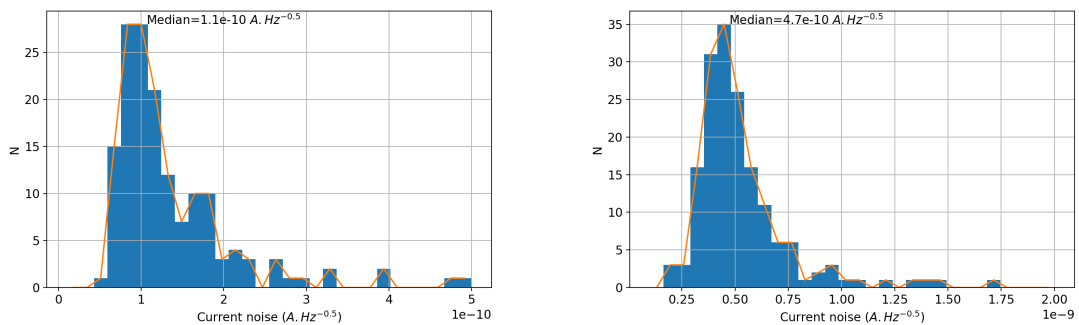


Figure 26. Histogram and density of current noise measured between 1 Hz and 2 Hz in the normal state (left, 153 total number of TES) and in the superconducting state (right, 146 total number of TES).

4.8.2 Noise in the transition

Figure 27 shows some typical current noise power spectra at different bias voltages. There is clear evidence of a noise increase at low frequency when decreasing the bias voltage, which is usually produced by the phonon noise in the TES. The noise level is however much higher than expected, and it varies between the TES, as seen in Figure 27.

A test of sensitivity to pulse tube (PT) microphonics was carried out by stopping the two units for a few minutes. An example timeline and associated time-frequency analysis is shown in Figure 28. The low frequency part of the noise level is reduced when both PTs are off, corresponding to the detector bandwidth. The induced parasitic signal is therefore thermal on the detector.

The current noise level can be further converted in NEP assuming the TES are in strong Electro-Thermal Feedback mode. In this case, the TES responsivity $\Re[A/W]$ is given by the inverse of the TES voltage, $\Re = \frac{1}{V_{TES}}$. The TES voltage is obtained from the bias voltage assuming the TES resistance is higher than the shunt resistance: $V_{TES} = V_{bias} \times 10^{-6}$.

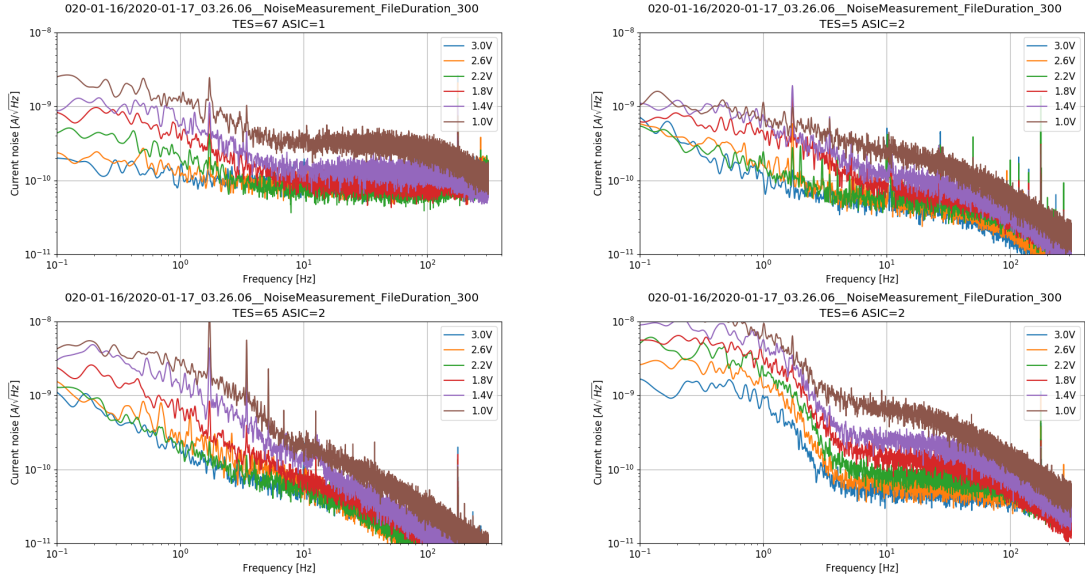


Figure 27. Spectra of the measured current noise on some channels at different bias voltages, from 3 V to 1 V. This corresponds to the ratio of TES and normal resistance ranging from about 60% to about 10%. Note that these measurements were taken at higher frequency sampling by choosing only rows 1 to 8, so $N_{MUX} = 32$ which leads to $f_s = 625$ Hz.

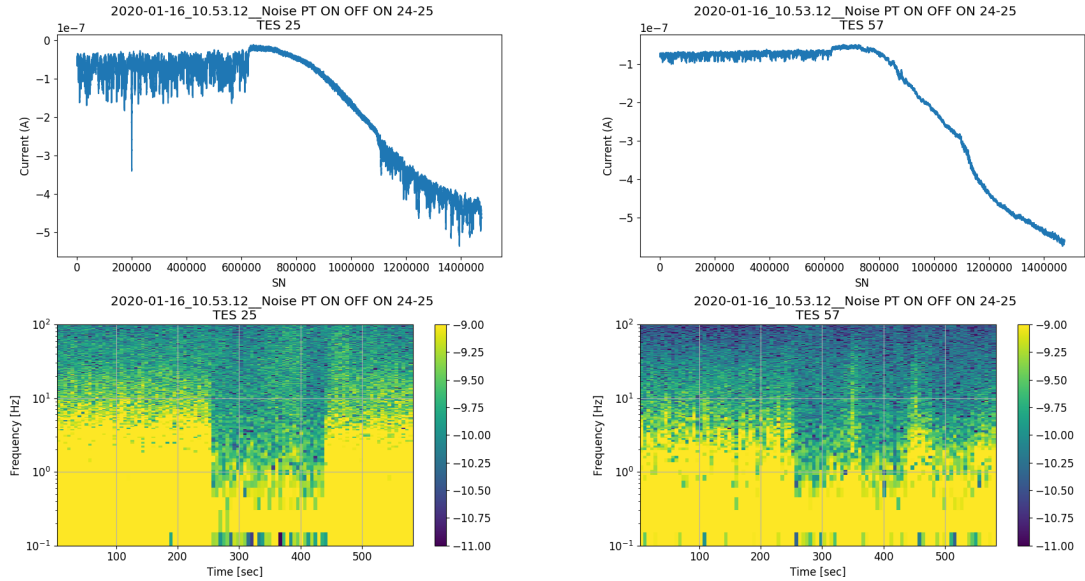


Figure 28. Examples of timeline in serial number SN units (sampling period of $400 \mu\text{s}$) and corresponding time-frequency analysis (in log of current noise) for two TESs. The two pulse tubes are OFF between ~ 240 s and ~ 420 s.

Figure 29 (left) shows the distribution in NEP for two cases: PTs on or off. It appears that the median NEP when the PT are on is about 3 times higher than when they are off. We are clearly dominated by the PT microphonics. The distribution of the NEP ratio between PTs on and off is presented in figure 29 right and figure 30 shows the degradation of noise because of the PTs on the TES array. It is not clear at this stage if we see here some

mechanical specific location on the wafer.

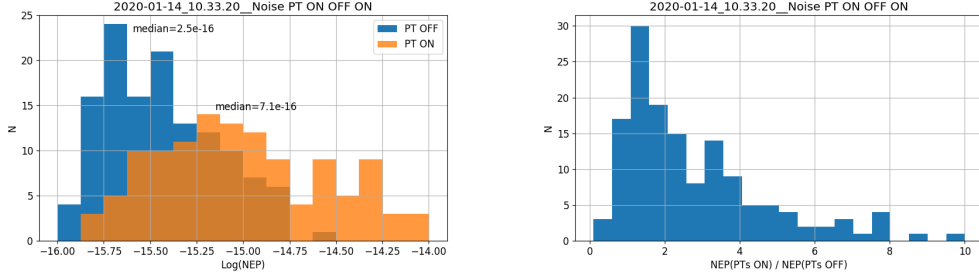


Figure 29. Left: Histogram of NEP measured between 1 Hz and 2 Hz in the transition ($V_{bias} = 1.5V$) with PTs ON and OFF. The response is assumed to be given by $1/V_{TES}$. The total number of TES are 130 and 120 respectively. Right: Histogram of the ratio of NEP with PTs ON and NEP with PT OFF. The total number of TES is 143.

The origin of these perturbations was investigated. We checked from temperature stability measurements that it is not due to thermal fluctuations of the TES or of the 1 K stage. The interpretation is the following: The pulse tube vibrations are exciting mechanical resonance on the TES support structure but also on the TES themselves. This mechanical resonance further dissipates heat on different parts of the system. This assumption is supported by 3 arguments:

1. In Figure 28 (right) after the PTs are switched off, we see a small increase in the TES current which is due to a small cooling of the detector, before heating up due to background increase.
2. We excited mechanically the cryostat with a speaker connected to an audio amplifier and a sine wave generator sweeping from 100 Hz to 1300 Hz in one hour. Figure 31 shows timelines of TES and of the TES stage thermometer as a function of the excited frequency. Resonances are clearly seen, especially around 700 Hz, probably due to a mechanical resonance.
3. With the same setup, we excited the cryostat at a resonance (251 Hz) but the sine wave is modulated in amplitude at 1.5 Hz with 50% depth. Figure 32 shows that this 1.5 Hz is seen directly by the TES. When changing the frequency of resonance (238 Hz for instance), the 1.5 Hz line disappeared from the TES spectra.

We are therefore seeing some heat dissipation produced mainly by the PT vibrations. The environment could also contribute to a lesser extent, for example the traffic on the road nearby.

A better mechanical decoupling of the two PTs is needed to overcome this problem. On the 40 K cold head, very soft copper braids will replace the current thermal strap to the 40 K shield. The 4 K cold head is already thermally connected to the 4 K shield with very soft copper braids. On the cryostat itself, a soft bellows between the PT and the structure can be added but this needs a detailed study. It should be noted that microphonics is a common problem for PT systems but the effect depends on the detailed mechanical configuration of the setup. This explains why such a strong effect was not seen at the sub-system level. This effect is described by [11–13], and [14]

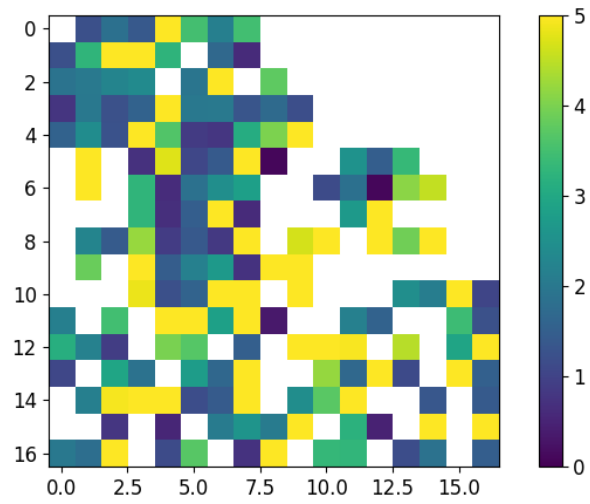


Figure 30. Map of the ratio of NEP with PTs ON and NEP with PT OFF.

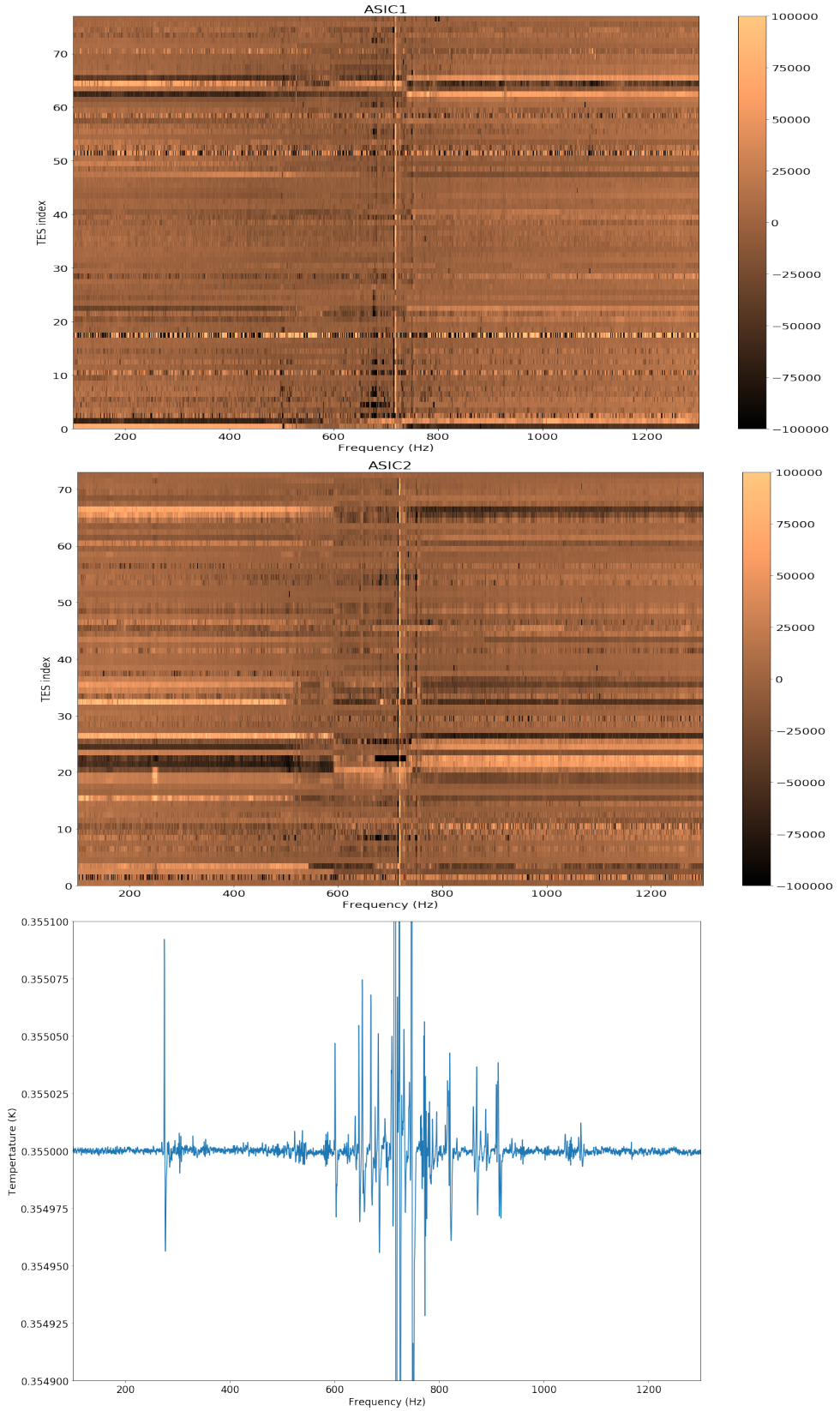


Figure 31. Top and middle: timelines in ADU of some TES as a function of the frequency of excitation. Bottom: Temperature of the TES stage as a function of the frequency of excitation. The graphs have been adjusted to share the same x-axis.

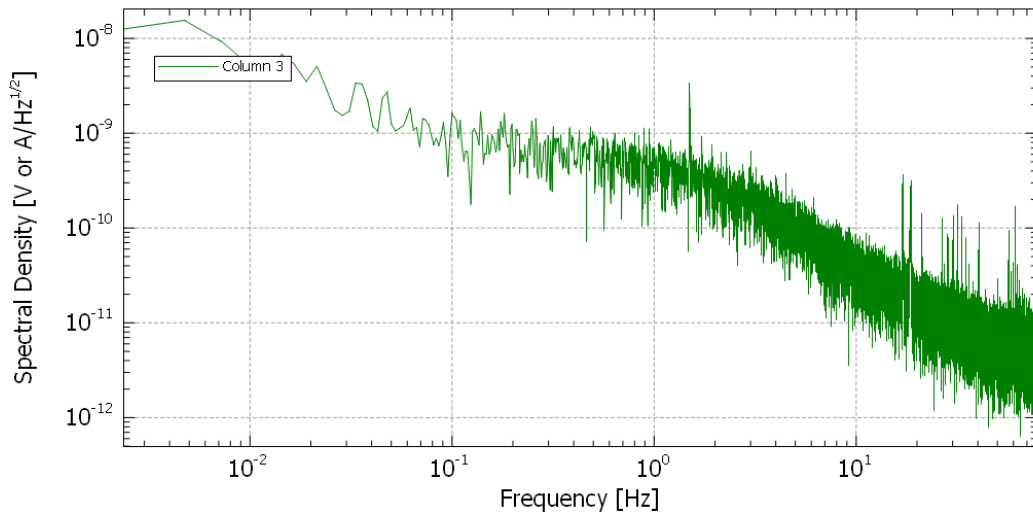


Figure 32. Spectra of TES 96 showing the 1.5Hz signal from the Amplitude Modulation of the mechanical excitation at 251Hz.

5 Conclusion

The QUBIC detection chain based on TES and SQUID, has reached an important milestone. We demonstrated an overall yield of 80% of working detectors (TESs and SQUIDs included), a thermal decoupling compatible with a phonon noise of $\sim 5 \times 10^{-17} \text{W}/\sqrt{\text{Hz}}$ at 410mK critical temperature, and a time constant of about 40ms which is enough for the instrument. The QUBIC sensitivity is however currently limited to $2 \times 10^{-16} \text{W}/\sqrt{\text{Hz}}$ by microphonic noise and aliasing in the readout electronics. The former will be soon improved by mechanically decoupling the first stages of the pulse tubes. The aliasing of the detector noise will be further improved by increasing the sampling frequency and adding Nyquist inductors to reduce the noise bandwidth of the detectors.

Acknowledgments

QUBIC is funded by the following agencies. France: ANR (Agence Nationale de la Recherche) 2012 and 2014, DIM-ACAV (Domaine d'Intérêt Majeur-Astronomie et Conditions d'Apparition de la Vie), CNRS/IN2P3 (Centre national de la recherche scientifique/Institut national de physique nucléaire et de physique des particules), CNRS/INSU (Centre national de la recherche scientifique/Institut national et al de sciences de l'univers). Italy: CNR/PNRA (Consiglio Nazionale delle Ricerche/Programma Nazionale Ricerche in Antartide) until 2016, INFN (Istituto Nazionale di Fisica Nucleare) since 2017. Argentina: MINCyT (Ministerio de Ciencia, Tecnología e Innovación), CNEA (Comisión Nacional de Energía Atómica), CONICET (Consejo Nacional de Investigaciones Científicas y Técnicas).

D. Burke and J.D. Murphy acknowledge funding from the Irish Research Council under the Government of Ireland Postgraduate Scholarship Scheme. D. Gayer and S. Scully acknowledge funding from the National University of Ireland, Maynooth. D. Bennett acknowledges funding from Science Foundation Ireland.

References

- [1] D. Prêle, F. Voisin, C. Beillimaz, S. Chen, M. Piat, A. Goldwurm, and P. Laurent, “SiGe Integrated Circuit Developments for SQUID/TES Readout,” *Journal of Low Temperature Physics*, vol. 193, pp. 455–461, Nov. 2018.
- [2] M. Salatino, B. Bélier, C. Chapron, D. T. Hoang, S. Maestre, S. Marnieros, W. Marty, L. Montier, M. Piat, D. Prêle, D. Rambaud, J. P. Thermeau, S. A. Torchinsky, S. Henrot-Versillé, F. Voisin, P. Ade, G. Amico, D. Auguste, J. Aumont, S. Banfi, G. Barbarán, P. Battaglia, E. Battistelli, A. Baú, D. Bennett, L. Bergé, J. P. Bernard, M. Bersanelli, M. A. Bigot-Sazy, N. Bleurvacq, J. Bonaparte, J. Bonis, G. Bordier, E. Bréelle, E. Bunn, D. Burke, D. Buzi, A. Buzzelli, F. Cavaliere, P. Chaniel, R. Charlassier, F. Columbro, G. Coppi, A. Coppolecchia, F. Couchot, R. D’Agostino, G. D’Alessandro, P. de Bernardis, G. De Gasperis, M. De Leo, M. De Petris, A. Di Donato, L. Dumoulin, A. Etchegoyen, A. Fasciszewski, C. Franceschet, M. M. Gamboa Lerena, B. García, X. Garrido, M. Gaspard, A. Gault, D. Gayer, M. Gervasi, M. Giard, Y. Giraud-Héraud, M. Gómez Berisso, M. González, M. Gradziel, L. Grandsire, E. Guerrard, J. C. Hamilton, D. Harari, V. Haynes, F. Incardona, E. Jules, J. Kaplan, A. Korotkov, C. Kristukat, L. Lamagna, S. Loucatos, T. Louis, A. Lowitz, V. Lukovic, R. Luterstein, B. Maffei, S. Masi, A. Mattei, A. J. May, M. A. McCulloch, M. C. Medina, L. Mele, S. Melhuish, A. Mennella, L. M. Mundo, J. A. Murphy, J. D. Murphy, C. O’Sullivan, E. Olivieri, A. Paiella, F. Pajot, A. Passerini, H. Pastoriza, A. Pelosi, C. Perbost, O. Perdereau, F. Pezzotta, F. Piacentini, L. Piccirillo, G. Pisano, G. Polenta, R. Puddu, P. Ringegni, G. E. Romero, A. Schillaci, C. G. Scóccola, S. Scully, S. Spinelli, M. Stolpovskiy, F. Suarez, A. Tartari, P. Timbie, M. Tristram, V. Truongcanh, C. Tucker, G. Tucker, S. Vanneste, D. Viganò, N. Vittorio, B. Watson, F. Wicek, M. Zannoni, and A. Zullo, “Performance of NbSi transition-edge sensors readout with a 128 MUX factor for the QUBIC experiment,” in *Millimeter, Submillimeter, and Far-Infrared Detectors and Instrumentation for Astronomy IX*, vol. 10708 of *Society of Photo-Optical Instrumentation Engineers (SPIE) Conference Series*, p. 1070845, July 2018.
- [3] S. Marnieros, P. Ade, J. G. Alberro, A. Almela, G. Amico, L. H. Arnaldi, D. Auguste, J. Aumont, S. Azzoni, S. Banfi, P. Battaglia, E. S. Battistelli, A. Baù, B. Bélier, D. Bennett, L. Bergé, J. P. Bernard, M. Bersanelli, M. A. Bigot-Sazy, N. Bleurvacq, J. Bonaparte, J. Bonis, A. Bottani, E. Bunn, D. Burke, D. Buzi, F. Cavaliere, P. Chaniel, C. Chapron, R. Charlassier, F. Columbro, A. Coppolecchia, G. D’Alessandro, P. de Bernardis, G. De Gasperis, M. De Leo, M. De Petris, S. Dheilily, L. Dumoulin, A. Etchegoyen, A. Fasciszewski, L. P. Ferreyro, D. Fracchia, C. Franceschet, M. M. Gamboa Lerena, K. Ganga, B. García, M. E. García Redondo, M. Gaspard, D. Gayer, M. Gervasi, M. Giard, V. Gilles, Y. Giraud-Heraud, M. Gómez Berisso, M. González, M. Gradziel, L. Grandsire, J. C. Hamilton, D. Harari, S. Henrot-Versillé, D. T. Hoang, F. Incardona, E. Jules, J. Kaplan, C. Kristukat, L. Lamagna, S. Loucatos, T. Louis, B. Maffei, W. Marty, S. Masi, A. Mattei, A. May, M. McCulloch, L. Mele, S. Melhuish, A. Mennella, L. Montier, L. Mousset, L. M. Mundo, J. A. Murphy, J. D. Murphy, F. Nati, E. Olivieri, C. Oriol, C. O’Sullivan, A. Paiella, F. Pajot, A. Passerini, H. Pastoriza, A. Pelosi, C. Perbost, M. Perciballi, F. Pezzotta, F. Piacentini, M. Piat, L. Piccirillo, G. Pisano, M. Platino, G. Polenta, D. Prêle, R. Puddu, D. Rambaud, P. Ringegni, G. E. Romero, M. Salatino, J. M. Salum, A. Schillaci, C. Scóccola, S. Scully, S. Spinelli, G. Stankowiak, M. Stolpovskiy, A. Tartari, J. P. Thermeau, P. Timbie, M. Tomasi, S. Torchinsky, G. Tucker, C. Tucker, D. Viganò, N. Vittorio, F. Voisin, F. Wicek, M. Zannoni, and A. Zullo, “TES Bolometer Arrays for the QUBIC B-Mode CMB Experiment,” *Journal of Low Temperature Physics*, vol. 199, pp. 955–961, Jan. 2020.
- [4] D. Prêle, M. Piat, L. Sipile, and F. Voisin, “Operating point and flux jumps of a SQUID in flux-locked loop,” *IEEE Transactions on Applied Superconductivity*, vol. 26, no. 2, pp. 1–5, 2016.
- [5] D. Prêle, F. Voisin, M. Piat, T. Decourcelle, C. Perbost, C. Chapron, D. Rambaud, S. Maestre,

- W. Marty, and L. Montier, “A 128 Multiplexing Factor Time-Domain SQUID Multiplexer,” *Journal of Low Temperature Physics*, vol. 184, pp. 363–368, Jul 2016.
- [6] J. Aumont *et al.*, “QUBIC Technical Design Report,” *arXiv e-prints*, p. arXiv:1609.04372, Sep 2016.
- [7] C. Perbost, “TES arrays for the detection of cmb b-mode polarisation : application to the QUBIC experiment,” *Archives Ouvertes*, Dec 2016.
- [8] J. C. Mather, “Bolometer noise: non equilibrium theory,” *Applied Optics*, vol. 21, pp. 1125–1129, Mar. 1982.
- [9] S. Marnieros *et al.*, “TES bolometer arrays for the QUBIC B-mode CMB experiment,” in *18th International Workshop on Low Temperature Detectors*, Jul 2019.
- [10] S. A. Torchinsky *et al.*, “QUBIC – III: Laboratory Characterization,” *J. Cosmo. Astroparticle Phys.*, vol. ?, p. ?, Oct 2020. in preparation.
- [11] S. R. Dicker *et al.*, *MUSTANG: 90 GHz science with the Green Bank Telescope*, vol. 7020 of *Society of Photo-Optical Instrumentation Engineers (SPIE) Conference Series*, p. 702005. 2008.
- [12] C. D. Sheehy *et al.*, *The Keck Array: a pulse tube cooled CMB polarimeter*, vol. 7741 of *Society of Photo-Optical Instrumentation Engineers (SPIE) Conference Series*, p. 77411R. 2010.
- [13] R. Maisonobe, J. Billard, M. De Jesus, A. Juillard, D. Misiak, E. Olivieri, S. Sayah, and L. Vagneron, “Vibration decoupling system for massive bolometers in dry cryostats,” *Journal of Instrumentation*, vol. 13, p. T08009, Aug 2018.
- [14] L. Gottardi, H. van Weers, J. Dercksen, H. Akamatsu, M. P. Bruijn, J. R. Gao, B. Jackson, P. Khosropanah, J. van der Kuur, K. Ravensberg, and M. L. Ridder, “A six-degree-of-freedom micro-vibration acoustic isolator for low-temperature radiation detectors based on superconducting transition-edge sensors,” *Review of Scientific Instruments*, vol. 90, p. 055107, May 2019.